

ETD Archive


---

2018

## Non-Intrusive Optical Measurement of Electron Temperature in Near Field Plume of Hall Thruster

Peter J. Urban  
*Cleveland State University*

Follow this and additional works at: <https://engagedscholarship.csuohio.edu/etdarchive>

 Part of the [Aerospace Engineering Commons](#), and the [Mechanical Engineering Commons](#)

[How does access to this work benefit you? Let us know!](#)

---

### Recommended Citation

Urban, Peter J., "Non-Intrusive Optical Measurement of Electron Temperature in Near Field Plume of Hall Thruster" (2018). *ETD Archive*. 1041.

<https://engagedscholarship.csuohio.edu/etdarchive/1041>

This Thesis is brought to you for free and open access by EngagedScholarship@CSU. It has been accepted for inclusion in ETD Archive by an authorized administrator of EngagedScholarship@CSU. For more information, please contact [library.es@csuohio.edu](mailto:library.es@csuohio.edu).

NON-INTRUSIVE OPTICAL MEASUREMENT OF ELECTRON TEMPERATURE IN  
NEAR FIELD PLUME OF HALL THRUSTER

PETER J. URBAN

Bachelor of Science in Mechanical Engineering

Case Western Reserve University

May 2013

submitted in partial fulfillment of the requirements for the degree

MASTER OF SCIENCE IN MECHANICAL ENGINEERING

at the

CLEVELAND STATE UNIVERSITY

May 2018

We hereby approve this Master's thesis

For

Peter J. Urban

Candidate for the Master of Science in Mechanical Engineering degree  
for the Department of Mechanical Engineering

And

CLEVELAND STATE UNIVERSITY'S

College of Graduate Studies

---

Dr. Antonie J. van den Bogert, PhD

---

Department & Date

---

Dr. Wei Zhang, PhD

---

Department & Date

---

Dr. Asuquo B. Ebiana, PhD

---

Department & Date

---

Dr. George J. Williams Jr., PhD

---

Department & Date

---

04-25-2018

---

Student's Date of Defense

## ACKNOWLEDGEMENTS

The author wishes to acknowledge the following individuals and institutions:

I would like to thank Dr. George Williams for providing advice, support, and mentorship provided during the course of this study. He was instrumental in the pursuit of my degree. Hopefully this work will be as useful to him as he was to me.

In addition, I would like to thank Dr. Maria Choi for her advice on how credible various electron temperature profiles were during initial stages of analysis. The staff of NASA Glenn's Electric Propulsion Lab must be acknowledged as well, for their professional advice and willingness to allow me to take data during their testing.

The institutional opportunity to conduct this research is thanks to NASA Glenn Research Center via the NASA internship program, and as such I hope that this information might be of some utility to them as an institution.

Cleveland State University and all its members also deserves to be acknowledged for providing me with the opportunity for post-graduate education. The staff has been kind, the campus enjoyable, and the education quality.

Finally, I wish to thank all my family members and friends. My parents have been nothing but supportive and encouraging, which was key in being certain I had made the right choice to leave my previous job to pursue a graduate degree. My friends have been great at providing me with diversion when needed and encouragement when required.

NON-INTRUSIVE OPTICAL MEASUREMENT OF ELECTRON TEMPERATURE IN  
NEAR FIELD PLUME OF HALL THRUSTER

PETER J. URBAN

**ABSTRACT**

Currently there is a large interest in the use of more efficient means of propulsion in long term missions due to the costs and difficulties associated with placing and maintaining the needed fuel for conventional chemical systems in orbit. Mass reduction of upper stages will return large returns due to the great reduction in required lower stage fuel. Due to these factors, alternatives are undergoing active research, though this paper is concerned with the area of electrical propulsion.

Electric propulsion is broadly defined as propulsion where the energization of the exhaust occurs via application of electromagnetic fields as opposed to chemical reactions or thermal processes. Frequently plasmas are involved in such processes, and as such, diagnostics related to establishing the characteristics of plasmas are of great value to the field, especially any techniques which do not disrupt the plasma in testing.

This study focused on the use of non-intrusive optical techniques to measure electron temperature in the near field of a Hall thruster, a type of electric propulsion. Results indicate that the pursued technique may be of utility to providing a simple to set up and execute diagnostic for determining electron temperatures in the near field of a hall thruster. This will allow for less-expensive rapid turnaround on obtaining of experimental data to test or provide as input for models of plasma behavior, wear in electric propulsion, thruster design, and operation confirmation.

## TABLE OF CONTENTS

	Page
ABSTRACT .....	iv
LIST OF TABLES .....	vii
LIST OF FIGURES.....	viii
NOMENCLATURE .....	x
CHAPTER	
I. INTRODUCTION .....	1
1.1 Background.....	1
1.2 Mass Savings Derivation.....	13
1.3 ITAR.....	17
II. THEORY .....	18
2.1 Fundamental Atomic Spectral Emission Overview.....	18
2.2 Collisional Radiative Model.....	20
2.3 Bulk Velocity Drift Correction.....	25
2.4 Abel Inversion .....	29
III. EXPERIMENTAL FACILITY .....	32
3.1 Thruster Setup.....	32
3.2 Thrust Stand.....	33
3.3 Vacuum Chamber .....	33
3.4 Power-Supply and Control Systems.....	33
3.5 Flow System .....	34
3.6 TDU-3.....	34
3.7 Instrumentation System .....	35
3.8 Calibration and Alignment .....	35
IV. DESCRIPTION OF EXPERIMENT .....	37
4.1 Residuals and Electron Temperature Calculation .....	38
4.2 Data Processing .....	41
V. RESULTS AND DISCUSSION .....	43
5.1 300V 75%B .....	44
5.2 300V 125%B .....	45

5.3	Comparable Data .....	48
5.4	General Observations .....	50
5.5	Diagnostic Utility .....	52
5.6	Error Discussion .....	55
VI. CONCLUDING REMARKS .....		64
REFERENCES .....		67
APPENDICES .....		71
A.	Additional Data .....	72
B.	Complimentary Diagnostic Proposal .....	74
C.	MATLAB Code.....	78

## LIST OF TABLES

Table	Page
I. Absorption Wavelengths .....	77



## LIST OF FIGURES

Figure	Page
1. Deep Space Gateway and Transport Plan.....	12
2. Intensity Ratio vs. Electron Temperature. ....	24
3. Intensity Ratio vs. Electron Temperature. ....	24
4. Energy Distributions.....	28
5. Thrust Stand Setup.....	32
6. Operating Hall Thruster.....	32
7. Data Collection Plane.....	35
8. Electron Temperature 300V 75%B, 3 Line, Fourier.....	45
9. Electron Temperature 300V 75%B, 3 Line, h-interpolation.....	45
10. Electron Temperature 300V 125%B, 3 Line, Fourier.....	47
11. Electron Temperature 300V 125%B, 3 Line, h-interpolation.....	47
12. Comparison Data, 300V 30kW.....	48
13. Comparison Data, 300V 10 kW.....	48
14. Comparison Data, 300V 10 kW & 300V 15 kW, Channel Centerline.....	48
15. Comparison Data (Simulation), 600V 12.5 kW.....	49
16. Single Able Inversion Error.....	55
17. 300V 75%B Lower Bound, Fourier.....	58
18. 300V 75%B Upper Bound, Fourier.....	58
19. 300V 75%B Lower Bound, h-interp.....	59
20. 300V 75%B Upper Bound, h-interp.....	59
21. 300V 125%B Lower Bound, Fourier.....	60
22. 300V 125%B Upper Bound, Fourier.....	60

23. 300V 125%B Lower Bound, h-interp.....	61
24. 300V 125%B Upper Bound, h-interp. ....	61
25. Comparative Electron Temperature.....	73

## NOMENCLATURE

### Symbols

- $\alpha$  = Ratio of singly ionized atoms to electrons
- $\lambda$  = Wavelength, m
- $\zeta^\lambda$  = Metastable population coefficient for given wavelength
- $\eta$  = Electrical generation efficiency
- $\sigma_{e0}^\lambda$  = Cross section of an electron exciting an atom, such that an atom will be excited from a lower state to one which will produce an emission with wavelength  $\lambda$ , m<sup>2</sup>
- $\sigma_n^\lambda$  = Cross section of an ion with ionization n, such that an atom will be excited from a lower state to one which will produce an emission with wavelength  $\lambda$ , m<sup>2</sup>
- $A_n$  = Fourier method constant for expansion term n
- $c$  = Speed of light, 299792458 m/s
- $C_{J \text{ to } eV}$  = Conversion factor,  $6.241509 \cdot 10^{18}$  eV/J
- $B$  = Magnetic field strength, Tesla
- $E_{field}$  = Electric field strength, volts/m
- $E_e$  = Electron energy, eV
- $\Delta E_e$  = Energy difference due to drift velocity, eV
- $f_e$  = Normalized electron energy distribution function
- $G$  = Universal gravitational constant,  $6.67408 \cdot 10^{-11}$  m<sup>3</sup> kg<sup>-1</sup> s<sup>-2</sup>
- $g_0$  = Acceleration due to gravity at surface of the Earth, 9.80665 m s<sup>-2</sup>
- $h$  = Planck's constant,  $6.62607004081 \cdot 10^{-34}$  kg m<sup>2</sup>/s
- $I_\lambda$  = Emission intensity at wavelength  $\lambda$
- $k_B$  = Boltzmann constant,  $8.61733035 \cdot 10^{-5}$  eV/K

- $k_{e0}^\lambda$  = Emission excitation rate coefficient for electron collisions with particles in ground state for  $\lambda$   
 $k_n^\lambda$  = Emission excitation rate coefficient for n-ionized collisions with particles for wavelength  $\lambda$   
 $K^\lambda$  = Metastable population coefficient for given  $\alpha$  and electron temperature for wavelength  $\lambda$   
 $m_A$  = Atomic mass, xenon,  $1.2230 \cdot 10^{11}$  eV  
 $m_e$  = Electron rest mass,  $5.1100 \cdot 10^5$  eV  
 $N_e$  = Number, electrons  
 $N_n$  = Number, n-ionized atoms  
 $r$  = Radial coordinate, m  
 $R$  = Radius of thruster, m  
 $T_e$  = Electron temperature, K  
 $v_{elec}$  = Electron velocity, m/s  
 $v_{elec,d}$  = Electron bulk drift velocity, m/s  
 $x$  = Linear coordinate  
 $y$  = Linear coordinate

# **CHAPTER I**

## **INTRODUCTION**

### 1.1 Background

#### 1.1.1 General Spaceflight Concerns

Space is a rather harsh environment for any object, and as such, safety, durability, and predictability are of utmost value to anyone wishing to design missions into space. Due to this, the understanding and modeling of all parts of the spacecraft are paramount. For example, the low pressure of a vacuum causes many types of lubricant to evaporate, rendering them useless in their intended their role. Large temperature differentials can cause differential stress on critical framework, or simply cause fatigue from cycling between extremes on every orbit through a shadow. Pressure differentials between the internal sections, if crewed and thus requiring an internal atmosphere, and the exterior of the craft place additional stresses on the structure. Many assumptions of design revolve around ‘down’ being meaningful in the same manner as earth, which is not the case in micro-gravity, more generalized definitions are of utility. This is leaving aside the dangers of micrometeorites, hairline fractures, extreme UV exposure, and other environmental hazards. Thanks to these facts, components are tested extensively, behavior is simulated in extreme detail, and contingency plans are numerous. Due to this any technique

that allows for more flexibility, reduced cost, or new capability in data collection is of great interest to space technology development.

Another major concern is the cost of putting objects into orbit. The most difficult part of any space mission is putting a craft into initial orbit in the existential sense. This is due to the energy needed to escape, or climb up, the gravity well of a planet, which can be calculated by the integration of potential energy from the surface of the earth out to infinity. From this an escape velocity can be calculated, and thanks to rocket equations, we can determine the amount of fuel needed to attain this velocity. The end result is that any reduction in required mass of upper stages provides enormous benefits in the reduction of required fuel on lower stages. The consequence of this is that technologies that allow for less required mass to accomplish the same goal are important for the increased viability of missions or space based applications.

In longer flights another matter of concern arises, the total amount of time that a mission will take to complete. While in general the reduction of time required is a desirable goal, it takes on new levels of importance when space exploration is involved. There is the most straightforward and obvious reason of course: the longer it takes for a craft to reach a destination, the longer it will take for useful data to be returned or a desired action to occur. The benefits of addressing this concern are quite obvious and straightforward. However, there is another major aspect that comes with transit time in space, specifically exposure to radiation. Thanks to the charged particles that are present in the solar system due to the sun, there is the constant accumulation of low level damage to electronics and other systems. While over the short term this is minor, given the mission lengths involved this is a cumulative process that can have rather large effects, with electronics being some of the most sensitive to this process. These effects extend to biological systems as well, meaning that flight time is a very large

factor in astronaut health, since it is controlling exposure time to whatever amount of radiation is able to penetrate the shielding in place. Thus, any technology that decreases flight time is not only of logistical concern, but health and human safety as well.

One more aspect that may not be obvious at first glance is thermal control. The first aspect that must be addressed is ensuring that any equipment, and internal environments if crewed, is warm enough to function properly. Low temperatures can cause parts to seize if moving parts are utilized, any residual moisture to freeze in unexpected locations, part embrittlement, and damage from differential material thermal contraction. Many of these concerns are hard to address without providing a thermal source on the craft or satellite, especially since the craft might see radically different temperatures during its operational lifespan. Less obvious, given the cold temperature of space, is thermal buildup. This is due to the fact that convection and conduction are not available to establish a thermal pathway. Due to this, heat only slowly leaves an object in space, which means any source of heat generation is potentially a large concern. In theory it would not be too hard to raise the temperature to the point that the craft, its cargo, or its occupants are endangered by said temperature. There are a number of ways to address this. Thermal sinks can be incorporated, the radiative surface area to volume ratio can be maximized, and less thermally sensitive materials can be used. However, the best way to address a problem usually is to work on root causes, in this case heat generation. One of the largest potential sources of heat is the source of propulsive thrust. For example, a chemical rocket works via exothermal chemical reactions, and the resultant hot gas is directed out of the craft via a physical nozzle. Due to the fact that the gas is in physical contact with part of the vessel, there is ample opportunity for thermal energy to transfer from the gas to the structure of the engine. In many cases, to prevent structural failure this heat must

be transferred away from the nozzle faster than radiative emission would cool it, and as such, there is net thermal buildup in the craft. Frequently, fuel and/or oxidizer can be used as a heat sink for this buildup, but it still means that additional thermal regulation systems must be incorporated. It also can limit burn times if the capacity to deal with heat buildup is insufficient. In addition, the sudden heating of components, even if ultimately the system is capable of dealing with such conditions, can lead to material fatigue, reducing its capacity to deal with high levels of stress in the future.

### 1.1.2 Electric Propulsion

Electric propulsion is the use of electrical power to energize the exhaust of a thruster as supposed to more conventional means such as chemical reaction or less conventional thermal processes. There are a number of types of electric propulsion, but this study focuses on Hall thrusters, so others will not be discussed in detail. Of note is that all currently extant electric propulsion systems are high efficiency in terms of propellant use but low thrust in their general performance, making them infeasible for launch stages and typically a poor choice for orbit escape if short time spans are required, though highly useful if time is less of an issue. Their high specific impulse, which is useful in station keeping and orbital transfers, is what makes investigation of their operation and optimization something that has potential for good returns on investigation [1].

Another interesting characteristic of electric propulsion systems is that they typically have very low propellant consumption rates, as one would expect from a high specific impulse device. While it is true that on missions the overall total impulse, the integral of thrust over total burn time, is what determines the change in velocity a system is capable of delivering, electrical propulsion is capable of providing this impulse for a much lower propellant mass



cost than chemical propulsion. However, the low thrust of such systems must be kept in mind for mission design, as this means that the same change in velocity that a chemical thruster might provide will be done in a larger span of time than said chemical thruster. That having been said, extended continuous burns are possible thanks to their low propellant consumption and high specific impulse, and are in fact the default for craft equipped with such a device as main propulsion. A continuous burn is highly desirable, since it means an orbit transfer can be done either much more efficiently in terms of propellant, much quicker in theory, or a lesser combination of the two. Even though their thrust is quite low, the fact that they can be operated for long periods of time means that the effects are quite notable for any long duration mission. In addition, it makes them quite well suited for station keeping. Minor perturbations of an orbit are inevitable, so correction will always be required. However, since it is not desirable to bring large stocks of fuel due to the mass involved, high propellant efficiency correction is of great utility.

In addition, there is another useful property of electric propulsion, one which is related to its name. Unlike chemical propulsion, which gets its power from stored chemical energy, electric propulsion can provide energy to exiting exhaust via processes powered by electricity. While this may not seem too relevant at first, there are highly weight efficient means of providing electrical power to a spaceship for certain mission profiles. The two largest possibilities for an increase in overall efficiency are solar and nuclear power generation. Solar of course is gathering ambient energy from light emitted from the sun, thus a device can utilize this to provide power with minimal cost in mass. The spacecraft does not need to bring its power with it, and it does not need to have as large and massive support and storage systems. However, the device is at the mercy of the light from the sun. Greater distance from the sun

means less energy can be produced, and production stops when solar panels are cast into shadow.

Nuclear power is currently not used for powering spacecraft, with the exception of batteries powered by nuclear decay. That said, due to the efficiency of power generation via nuclear fission, a comparatively very small amount of fuel can provide a large amount of electrical power for an extremely extended period of time. In fact, the amount of power provided can be throttled to match the current needs of a spacecraft. The downside of course is that extensive support structure is required to control the reaction, extract energy from heat, and vent waste heat. This has a very large mass cost, so further research is required to make this method of power provision truly viable, though it has great potential benefits if the challenges can be met. There are also the downsides of any nuclear-powered device, with the exception of waste thanks to the fact that either it is a fully self-contained item which will be decommissioned before refueling is required or said waste can be placed in a trajectory which will safely dispose of the offending material.

Relating to the thermal concerns outlined in the section on general issues in spaceflight, electrical propulsion has an advantage over chemical rockets. Cryogenic temperatures do not need to be maintained in regards to the propellant. This makes it much easier to engineer means to address the required heat regulation. These easier solutions are also more likely to take less mass to implement, which increases the overall efficiency of the mission further still.

### 1.1.3 Hall Thrusters

Hall thrusters are a type of electric propulsion that have potential application in number of applications, with the Advanced Electric Propulsion System, AEPS for short and the program which generated data collected in this study, intended for primary propulsion applications.

They potentially have a specific impulse range of 1000-3000 s or higher, and much lower thrust than a typical chemical rocket engine. It means that much less mass is needed for most operations due to this increased efficiency. For the intended application of the AEPS, high  $I_{sp}$  allows for high change in velocity per overall mass of the propulsion system, which is notably higher than chemical propulsion methods. In pursuit of the goals of AEPS, the Hall Effect Rocket with Magnetic Shielding (HERMeS) is receiving continued testing, wear reduction support, and insight from NASA and JPL [2, 3, 4]. HERMeS has a rather extensive set of requirements for parameter range and operational lifespan, and thus large amounts of testing to better understand its behavior and reduce wear is currently being undertaken [5].

The basic concept of a Hall thruster is that a gas, usually xenon, is ionized in a concentric channel and then these ions are accelerated out of the thruster to generate thrust. Said acceleration is possible due to local electrical fields that are induced in the plasma of the thruster. When a force is applied to a charged particle perpendicular to the magnetic field, there is an induced velocity that is perpendicular to both the magnetic field and force. It is rather important that the induced electron current from this effect does not impact a wall, or else the life span and efficiency of the device will be much less due to loss of electron confinement. Thus, the use of cylindrical geometry, since this makes it much easier to ensure no impact occurs; the channel is in the direction of the induced drift. [6]

The magnetic field of a Hall thruster is established by use of electromagnetics, with the specifics of the field determined by the needs of maximizing performance of the device and reducing impact with the walls of the thruster. The electric field is induced via the use of flowing electrons from a negatively charged cathode to a positively charged anode in addition to induced local plasma potentials. The flowing electrons also has the positive benefit of

providing a means to ionize the gas via collision of the electrons with the neutral gas. Said ions then are extracted from the plasma's ionization zone and accelerated away from the thruster, thus providing the means by which a thrust can occur. [6]

As mentioned, the magnetics of a Hall thruster also can be used to reduce impact of ions with the walls of the channels. Ions impact the walls due to the distribution of plasma potentials and electron temperatures that can change local potentials [6], which can be affected by the magnetic field. Careful manipulation of the magnetic field can be utilized to shield the walls from ion impacts by forcing plasma potentials along the walls to be approximately constant, which reduces the wear done to the walls due to the fact constant potential would prevent acceleration towards the walls. This reduced wear then means increased service life for the thruster, thus it can be relied upon more for propulsive needs, increasing the overall efficiency of the spacecraft.

This concept of this magnetic shielding was developed based on simulation data [5] and later proof of concept investigation [5]. Magnetically shielded Hall thrusters have been shown to have a reduction in the wear of the channels by a significant amount [5], however it was observed that wear of the cover of the central hub of the thruster was still occurring due to bombardment from high energy xenon ions [2]. Due to this, more investigation into the behavior of the plasma and thruster is required.

#### 1.1.4 Plume Characterization

Currently plasma physics and the proper means to computationally model them are still not understood to the point that all properties can be predicted with high precision in sufficiently complex or turbulent systems, such as occurs in Hall thrusters, so additional information on plume characteristics is required to go to higher powers and properly model service life. Since

current modeling alone is not sufficiently accurate, extensive empirical data collection is required to ensure that thruster and wear behavior is properly understood. For example, the specifics of how a plasma varies sufficiently close to a thruster as parameters are changed requires more investigation. However, there is a number of issues with the currently utilized means of collecting this data. Physical probes will cause perturbation of the high-density plasma near the thruster and will yield incorrect measurements. Laser-induced fluorescence does not cause physical perturbation in the manner of physical probes but is expensive and can be potentially intrusive to test configurations. As such, new types of diagnostics need to be developed and validated to overcome these downsides, or provide complimentary means of data collection so that enough techniques exist to cover the weaknesses of other diagnostics.

Testing electrical propulsion devices is expensive: large quantities of xenon gas must be acquired and stored, sufficiently large vacuum chambers must be maintained, and a device with a power draw in the tens of kilowatts must remain on for extended periods. In addition, the testing time requires a large amount of manhours. Given the expensive nature, any savings in plume characterization would be useful for reducing the cost of validation and characterization which in turn would decrease the overall price tag of electric propulsion systems. The setup used in this study required only an optical pick up, two simple movement stages, fiber optic cable, a spectrometer, and a computer. These items are common in laboratories performing research into plasmas, and even if were not on hand originally, can be reused in other forms of tests, making capital investment in the needed equipment much easier to justify. Even if ultimate data resolution that the diagnostic explored in this study turns out to be less than ideal for full characterization, it could act as a filter to determine areas that more in-depth techniques should be used.

In addition, easy to deploy and utilize diagnostics can allow for better evaluation of existing electric propulsion in space deployments. As previously mentioned, space is a harsh environment, one that is rather hard to replicate on Earth. Even the best quality vacuum chambers cannot fully replicate a space environment, since even if they were able to obtain the same pressures, it would be infeasible to exactly replicate the charged particles, radiation, and low gravity conditions. While many of these factors can be accounted for, or simulated to various degrees, there may be differences based upon assumptions used. Due to this, behavior in space might potentially be different than in ground testing, thus making any portable and easy to deploy diagnostic useful for fully understanding the properties of propulsion in current or future use.

To be specific, if it is possible to create a diagnostic that does not need to physically enter the plume, and is rugged and light enough to be brought on a launch into space, differences in the behavior of the thruster between ground based testing and intended operation in space could be examined in detail when opportunity arises. For example, inclusion of such a diagnostic on a satellite equipped with a Hall thruster for station keeping would be a feasible means to pursue this potential. The satellite need not be a dedicated mission for such examination if the diagnostic is low mass impact, it simply can be an addition to a satellite with a different unrelated mission. Given the comparative costs to place an object in orbit versus equipment production, it is likely that a low mass implementation will be prioritized over low cost of production.

#### 1.1.5 Electron Temperature

Temperature is normally considered a statistical quantity defined by the change in internal energy with respect to entropy where volume and particle number is held constant. However,

in statistical thermodynamics it is possible to define temperature in another manner. If a system is in thermodynamic equilibrium, or at least local equilibrium, then its statistical properties may be described by what is known as a partition function. A partition function is a function which describes the statistical characteristics of a system. [8] In a plasma, electrons have a distribution of velocities that is typically assumed to take on a Maxwellian distribution, though anisotropic conditions can result in non-Maxwellian distributions. This distribution has a parameter that scales the shape of the distribution, which is taken to be the temperature. This temperature of the distribution then is the electron temperature. In the context of plasma physics, this is commonly expressed in terms of electron volts, though it may be presented in terms of Kelvin as well. Many properties dependent on or are influenced by electron temperature, thus is important to understanding the plasma [6].

Because electron temperature is a measure of the energy distribution of the electrons in a plasma, this value is of great utility to a number of applications. For example, accurate knowledge of electron temperature is quite helpful in wear modeling, efficiency improvements, and ease of scaling. While fundamental plasma physics may be able to predict a large amount of behavior, high specificity in plasmas with sufficiently complex systems remains elusive in some instances; for example, in the near-field plasma of a Hall thruster. As such, empirical information is needed to further refine designs and models, even if the overall behavior can be ascertained and modeled from fundamental plasma physics.

#### 1.1.6 Phased Human Exploration Plan

NASA has publicly revealed its intended plan for a phased exploration concept on March 28, 2017 [9]. NASA presented the general architecture of its plan, shown in Fig. 1 to increase human presence in the solar system, including flight testing in cis-lunar space and validation

of crewed missions beyond the orbit of the moon. One of the major intents of this initiative is to achieve human exploration of Mars, thus technologies suited to such a push have been prioritized [10].

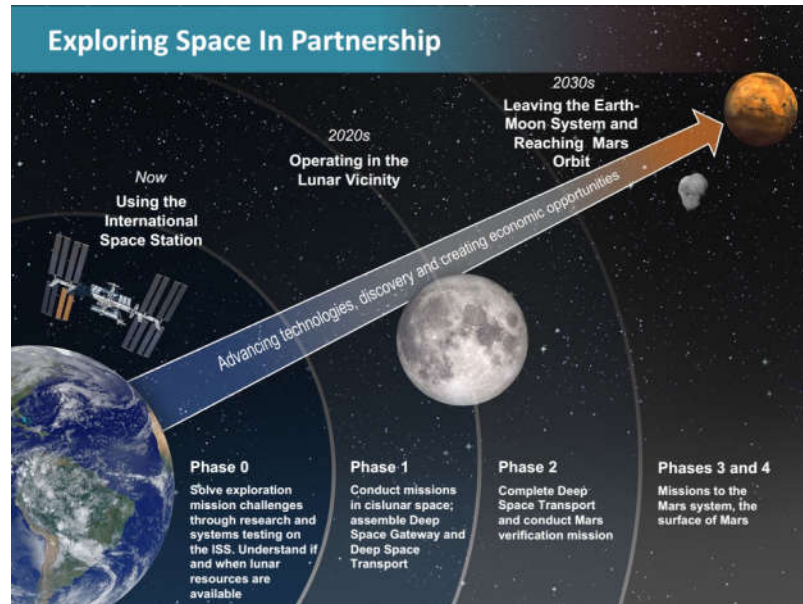


Fig. 1: Deep Space Gateway and Transport Plan [10]

Thus, the earlier discussed utility of electric propulsion for manned exploration is not purely theoretical, but has possibility of application to current intent. This means that techniques and diagnostics assisting in the development of electric propulsion would directly contribute to a coordinated effort in addition to providing general capacity to characterize the behavior of the systems involved.

Since there is a realistic potential application to manned spaceflight for a Hall thruster, testing and characterization is of a much higher priority than if only non-manned spaceflight was being considered. Due to the fact that human lives could be dependent on the performance of the system, a very thorough understanding of all behavior is required, and large margins of safety are needed. Because of this, any way to provide new reliable or less costly means of investigation will increase the chances of success of the initiative, either in the absolute sense



or by reducing cost to pave the way for sufficient understanding to confidently green light a design.

## 1.2 Mass Savings Derivation

To show the importance of increased specific impulse in a rocket, a simple derivation of the amount of work required to escape Earth orbit will be presented. This derivation is for a one-way escape trajectory from the Earth-Lunar system. That said, it can be expanded for any other type of mission by simply including the needed fuel for the remainder of mission in what is treated as the final mass.

The amount of work required to escape the gravity well of an object is the integral of the force of gravity from the initial position to infinity.

$$W = \int_{r_e}^{+\infty} G \frac{m_{earth}m_{rocket}}{r^2} dr \quad (1)$$

Instead we can find the work required per unit mass to determine a constant showing the importance of mass when launching from sea level for a 100% efficient engine:

$$W = \int_{r_e}^{+\infty} G \frac{m_{earth}m_{unit}}{r^2} dr = 6.24933 * 10^7 \frac{J}{kg} \quad (2)$$

This assumes that the entire mass of the rocket is sent to escape Earth orbit, which of course is not the case both due to use of fuel during launch and staging. Instead we can find the amount of change in velocity required for a given rocket:

$$\frac{1}{2}m_{rocket}v_{rocket}^2 = \int_{r_e}^{+\infty} G \frac{m_{earth}m_{rocket}}{r^2} dr = W \quad (3)$$

The mass of the rocket cancels out leaving:

$$v_{rocket} = \sqrt{2W_{unit}} = 11179.7 \frac{m}{s} \quad (4)$$

From here we can use the rocket equation [11] to demonstrate the importance of the efficiency of the propulsion system:

$$\Delta v_{rocket} = \frac{F_{thrust}}{\dot{m}} g_0 \ln \left( \frac{m_{original}}{m_{final}} \right) = I_{sp} g_0 \ln \left( \frac{m_{final} + m_{fuel}}{m_{final}} \right) \quad (5)$$

$$m_{final} e^{\left( \frac{\Delta v_{rocket}}{I_{sp} g_0} \right)} - m_{final} = m_{fuel} \quad (6)$$

Thus, the amount of fuel needed to achieve a given change in velocity is derived. However, since the escape velocity of Earth is known from Eq. 4, and the only two unknowns are the specific impulse and the final mass of a rocket. The final mass can be declared, as it will be the final payload. This leaves the specific impulse, which is a measure of its efficiency. As discussed in the introduction, the specific impulse of electrical propulsion is much greater than chemical propulsion. However, electric propulsion cannot be used to launch from the surface of the Earth to orbit, so instead a calculation of the change in velocity for escape from low earth orbit (LEO), here taken to mean 300km above the Earth's surface, is needed.

$$W = \int_{r_e+300km}^{+\infty} G \frac{m_{earth} m_{unit}}{r^2} dr = 5.96859 * 10^7 \frac{J}{kg} \quad (7)$$

$$v_{rocket} = \sqrt{2W_{unit}} = 10925.7 \frac{m}{s} \quad (8)$$

Note that this does not include the effects from using the Oberth effect or gravitational assist from the moon, which would decrease the total required change in velocity, but for the sake of simplicity, inclusion of utilization of these effects is not presented here. Then the velocity to attain LEO is calculated:

$$W = \int_{r_e}^{r_e+300km} G \frac{m_{earth}m_{unit}}{r^2} dr = 2.80739 * 10^6 \frac{J}{kg} \quad (9)$$

$$v_{rocket} = \sqrt{2W_{unit}} = 2369.55 \frac{m}{s} \quad (10)$$

However, this is not enough since this is only what is required to reach the altitude of LEO. Orbital speed must be achieved as well. Derivation proceeds by finding the needed centripetal force, then solving for velocity:

$$F = ma = \frac{mv_{rocket}^2}{r_e + 300km} \quad (11)$$

$$G \frac{m_{earth}}{r_e + 300km^2} = \frac{v_{rocket}^2}{r_e + 300km} \quad (12)$$

$$v_{rocket} = \sqrt{G \frac{m_{earth}}{r_e + 300km}} = 7725.67 \frac{m}{s} \quad (13)$$

From here the two speeds are added together to obtain the final needed change in velocity, giving a final number of 10095.22 m/s to achieve LEO. Now it is possible to calculate the amount of initial fuel needed to launch a rocket to escape velocity in two stages, one to LEO, the other from low earth orbit to escape:

$$\Delta v_{rocket} = I_{sp}g_0 \ln \left( \frac{m_{original}}{m_{LEO}} \right) \quad (14)$$

$$m_{LEO} + m_{staging} = \frac{m_{original}}{e^{\left( \frac{\Delta v_{rocket}}{I_{sp,launch}g_0} \right)}} \quad (15)$$

$$m_{final} = \frac{m_{LEO}}{e^{\left( \frac{\Delta v_{rocket}}{I_{sp,EP}g_0} \right)}} \quad (16)$$

$$m_{useful} + m_{electrical\ support} = \frac{m_{LEO}}{e^{\left( \frac{\Delta v_{rocket}}{I_{sp,EP}g_0} \right)}} \quad (17)$$

Rearrange and substitute through and it can be found:

$$m_{final} e^{\left(\frac{\Delta v_{rocket}}{I_{sp,EP} g_0}\right)} e^{\left(\frac{\Delta v_{rocket}}{I_{sp,launch} g_0}\right)} + m_{stg} e^{\left(\frac{\Delta v_{rocket}}{I_{sp,launch} g_0}\right)} = m_{original} \quad (18)$$

However, the original mass is simply the final payload plus the total fuel, both chemical and electrical required, along with staging thus:

$$m_{final} e^{\left(\frac{\Delta v_{rocket}}{I_{sp,EP} g_0}\right)} e^{\left(\frac{\Delta v_{rocket}}{I_{sp,launch} g_0}\right)} + m_{stg} e^{\left(\frac{\Delta v_{rocket}}{I_{sp,launch} g_0}\right)} = m_{final} + m_{fuel} + m_{stg} \quad (19)$$

So it is possible to solve for the total fuel required to achieve low earth orbit in such a configuration:

$$m_{final} e^{\left(\frac{\Delta v_{rocket}}{I_{sp,EP} g_0}\right)} e^{\left(\frac{\Delta v_{rocket}}{I_{sp,launch} g_0}\right)} + m_{stg} e^{\left(\frac{\Delta v_{rocket}}{I_{sp,launch} g_0}\right)} = m_{final} + m_{fuel,LEO} + m_{fuel,LEO,E} + m_{stg} \quad (20)$$

$$m_{final} e^{\left(\frac{\Delta v_{rocket}}{I_{sp,EP} g_0}\right)} e^{\left(\frac{\Delta v_{rocket}}{I_{sp,launch} g_0}\right)} + m_{stg} e^{\left(\frac{\Delta v_{rocket}}{I_{sp,launch} g_0}\right)} = m_{final} + m_{fuel,LEO} + \left( \frac{m_{original}}{e^{\left(\frac{\Delta v_{rocket}}{I_{sp,launch} g_0}\right)}} - m_{stg} - m_{final} \right) + m_{stg} \quad (21)$$

$$m_{final} e^{\left(\frac{\Delta v_{LEO,E}}{I_{sp,EP} g_0}\right)} e^{\left(\frac{\Delta v_{LEO}}{I_{sp,launch} g_0}\right)} + m_{stg} e^{\left(\frac{\Delta v_{LEO}}{I_{sp,launch} g_0}\right)} = m_{fuel,LEO} + m_{final} e^{\left(\frac{\Delta v_{LEO,E}}{I_{sp,EP} g_0}\right)} \quad (22)$$

$$m_{final} e^{\left(\frac{\Delta v_{LEO,E}}{I_{sp,EP} g_0}\right)} \left( e^{\left(\frac{\Delta v_{LEO}}{I_{sp,launch} g_0}\right)} - 1 \right) + m_{stg} e^{\left(\frac{\Delta v_{LEO}}{I_{sp,launch} g_0}\right)} = m_{fuel,toLEO} \quad (23)$$

However, it is important to recognize that the final mass includes the power support systems involved in the running of electrical propulsion. Thus, to get the amount of fuel required to bring a payload to orbit, one must split the final mass:

$$\left( m_{use} + m_{elec\ sup} \right) e^{\left(\frac{\Delta v_{LEO,E}}{I_{sp,EP} g_0}\right)} \left( e^{\left(\frac{\Delta v_{LEO}}{I_{sp,launch} g_0}\right)} - 1 \right) + m_{stg} e^{\left(\frac{\Delta v_{LEO}}{I_{sp,launch} g_0}\right)} = m_{fuel,toLEO} \quad (24)$$

Assuming a linear relationship between the power needed and the mass of the power systems, as well as a constant efficiency of the system [12]:

$$m_{elec\ sup} = \alpha P = \frac{\alpha W}{\eta \Delta t} = \frac{\alpha m u_e^2}{2 \eta \Delta t} = \frac{\alpha \dot{m} u_e^2}{2 \eta} = \frac{\alpha F u_e}{2 \eta} = \frac{\alpha F I_{sp} g_0}{2 \eta} \quad (25)$$

$$\left( m_{use} + \frac{\alpha F I_{sp} g_0}{2 \eta} \right) e^{\left(\frac{\Delta v_{LEO,E}}{I_{sp,EP} g_0}\right)} \left( e^{\left(\frac{\Delta v_{LEO}}{I_{sp,launch} g_0}\right)} - 1 \right) + m_{stg} e^{\left(\frac{\Delta v_{LEO}}{I_{sp,launch} g_0}\right)} = m_{fuel,toLEO} \quad (26)$$

Where  $\alpha$  is the constant of mass efficiency for a given power,  $F$  is the thrust of the Hall thruster,  $P$  is the power required,  $W$  is the total work needed,  $\Delta t$  is the time over which propulsion is provided,  $m$  is propellant mass,  $\eta$  is efficiency of power generation,  $u_e$  is the exit velocity of the propellant,  $\dot{m}$  is the mass flow rate, and  $F$  is the thrust of the system. Or to substitute back in exact numbers:

$$\left(m_{use} + \frac{\alpha F I_{sp} g_0}{2\eta}\right) e^{\left(\frac{10925.7}{I_{sp,EP} g_0}\right)} \left(e^{\left(\frac{10095.22}{I_{sp,launch} g_0}\right)} - 1\right) + m_{stg} e^{\left(\frac{10095.22}{I_{sp,launch} g_0}\right)} = m_{fuel,toLEO} \quad (27)$$

From this it can be seen that the amount of required fuel to achieve low Earth orbit is dependent on the final payload, and the specific impulse of the final electric propulsion and the thrusters used to achieve orbit. Unfortunately, there is not a monotonically decreasing relationship between specific impulse and required initial fuel to enter low earth orbit. However, better understanding of the behavior of the thruster would allow fine-tuning of the parameters of the thruster.

### 1.3 ITAR

Parts of the research in this thesis is covered under International Trade in Arms Regulations (ITAR), a United States regulatory regime intended to promote American national security interests and foreign policy. As such, some values and information cannot be presented in direct form. The main values to note that this is applicable to is dimensional information and magnetic field strength. Due to the fact they fall under ITAR's purview, they will be presented in normalized form to comply with regulations.

## **CHAPTER II**

### **THEORY**

#### 2.1 Fundamental Atomic Spectral Emission Overview

Atoms, including ones in their ionized states, tend to take the minimal stable energy configuration possible, the ground state, and deviations from this state require additional energy to be supplied [8]. The specific states, the configurations, available for atom to be in, as well as their energy requirements, is determined by fundamental quantum mechanics. Two potential ways of supplying the required energy to enter an excited state, or emitting energy to return to the ground state, is via photon absorption/emission and collisions [8, 12]. Of note is that in plasmas it is typical that most atoms are in an ionized state and that there is a population of free electrons [12]. For the purposes of this discussion “atom” in this section refers to both neutrals and ions unless otherwise specified.

The energy required to enter a state, or emitted to return to ground, via photon emission and absorption is, as mentioned, governed by quantum mechanics. In addition, the energy of a photon corresponds to its wavelength [8, 13]. Due to this there is no continuous distribution of wavelengths that may excite an atom nor be emitted by an atom transitioning to a lower energy state, but rather there is a discrete number of lines. Thus, every atom has a specific spectrum associated with its various excitations [13]. This means that the distribution of states

of a collection of excited atoms can be determined by the photons emitted.

However not all valid wavelengths are of equal intensity in an emission spectrum [13]. This is because for a given starting state there are a number of other states that the atom may transition to provided energy requirements are met. The probability of a transition occurring is governed by the properties of the two states in question, and typically expressed in what is known as an Einstein coefficient [13]. These can be either an expression of the probability of a spontaneous emission or absorption and stimulated emission. It is due to this differing probability and number of transitions that correspond to a specific wavelength that not all wavelengths will have equal intensity [13].

An additional complication arises in that there are some states that are not the ground state yet have no allowed transitions to a lower state. These are known as metastable states. Due to the presence of these states it cannot be assumed that all atoms will reach a ground state or are currently in the ground state if not in an excited state. Given that the metastable states have different transitions associated with them, the population of atoms in a metastable state will affect the emission and absorption spectrums of a larger population of atoms [13].

Further complicating matters is that photon emission and absorption is not the only means by which state transitions might occur. Collisions involving any combination of atoms that are ionized or in a neutral state and electrons can provide a means to change the energy state of a given atom [12]. The excitation rate coefficients corresponding to this can be expressed as a function of the energy distribution of the exciting or deexciting entity, the velocity of said entity, and a quantity known as the cross-section [14]. Please note that this cross-section is not the same as the physical cross-section of the items involved due to the fact that atomic and electromagnetic forces are involved.

Interestingly enough this means that the parameter typically called temperature can refer to several different quantities which can be rather different in a plasma. It can mean the kinetic energy of atoms and ions, the kinetic energy of free electrons, and the parameter scaling the shape of the energy distribution of a population. As previously discussed having more energy might correspond to a different state as supposed to having an increased velocity. In addition, due to the fact that there are free electrons, it is likely that their population and that of the atoms will have different velocity distributions. This is due to collisions between items of very different mass take a long time to reach kinetic equilibrium.

Finally, this means that models can be constructed to correlate the emission spectrum of a plasma to other properties of the plasma. For example, if one assumes that all deexcitation occurs via radiation or said radiative decay is much greater than deexcitation via collision, which is not justified for some transitions, one may relate the intensity of the emission lines to the relative density of the various excited states [14]. This can be coupled to the needed energy distributions to induce the observed state, and if states can be found that their density does not depend strongly on the energy distribution of ions, it is possible to relate the observed intensities of an emission spectrum to the energy distribution of the electrons once excitation from emission is taken into account [14]. How and if metastable populations are taken into account will affect the model used. A model that takes into account depopulation of metastable states via collision will be different than one that does not [14].

## 2.2 Collisional Radiative Model

Plumes in a Hall thruster consist of neutrals, ions, and electrons, where the ions are formed by collisions with electrons. These ions are then accelerated by electric fields in the thruster. During this process, collisions form excited states that will lead to optical emission that can



provide useful information on the state of the plasma. If we wish to know the electron temperature of a Hall thruster plume, one method to obtain this information is based on comparison of emission line intensities from atoms and ions excited out of the ground state [14]. However, to do this, we need to calculate the expected line intensities as they can be related to the electron temperature. The wavelengths of these emissions are determined by the energy gap between the starting state and ending state thanks to the fact that the energy of a photon can be determined from the wavelength alone. Based on the collisional radiative model for xenon outlined by G. F. Karabadzhak et al. [14] for 788.7 nm, 823.2 nm, 828.0 nm, 834.7 nm, 881.9 nm, 904.5 nm, 916.3 nm, and 980.0 nm emission lines, the following equations hold:

$$I_\lambda = \frac{hc}{4\pi\lambda} N_0 N_e \left[ \sum_p \frac{N_p}{N_0} \int_0^\infty v_{elec} f_e(E_e) \sigma_{ep}^\lambda(E_e) dE_e + \sum_q \frac{N_q}{N_0} \int_0^\infty v_{ion} f_q(E_q) \sigma_q^\lambda(E_q) dE_q \right] \quad (28)$$

$N_e$ ,  $N_q$ ,  $N_p$ ,  $N_0$  are the number of electrons, ions, xenon atoms in state  $p$ , and all xenon atoms. The first summation is for electrons, the second is for ions. The  $\sigma_n^\lambda(E_n)$  represents the cross section of an atom with charge  $q$  and energy  $E$ , or electron exciting an atom to state  $p$  with given energy  $E$ , such that an atom will be excited from a lower state to one which will produce an emission with wavelength  $\lambda$ .  $E$  is electron energy, and  $v$  is the velocity. The integrals are a calculation of the excitation rate coefficients, thus making the equation a summation of the contributions of the various states to the overall emission. These equations assume that excited states are depopulated through radiation only. This does not hold for all states, but so long as probability of spontaneous emission deexcitation is sufficiently greater than the collisional deexcitation of the plasma, the equation will hold. Since electron depopulation collision frequencies are so much higher than heavy particle depopulation collision frequencies, this condition can be stated as [14]:

$$A_i = \sum_k A_{ik} \quad (29)$$

$$A_i \gg N_e \int_0^{\infty} v_{elec} f_e(E_e) \sigma_{de}(E_e) dE_e \quad (30)$$

Where  $A_{ik}$  is Einstein coefficient of the  $i$  to  $k$  spontaneous emission transmission and  $\sigma_{de}$  is the electron collisional depopulation cross section for the upper  $i$ th level. This was found to hold in G. F. Karabadzhak et al's review of literature for Hall thrusters using xenon for the mentioned lines of interest [14]. Equation 24 can be consolidated and rewritten into:

$$I_\lambda = \frac{hc}{4\pi\lambda} N_0 N_e \left( \sum_p \frac{N_p}{N_0} k_{e0}^\lambda + \frac{N_1}{N_e} k_1^\lambda + \frac{N_2}{N_e} k_2^\lambda \right) \quad (31)$$

Where  $k_{e0}^\lambda$ ,  $k_1^\lambda$ , and  $k_2^\lambda$  are the emission excitation rate coefficients of ground state atoms, single ionized, and doubly ionized ions respectively. From here the emission excitation rate coefficients are calculated with the assumption of a Maxwellian electron energy distribution,  $f_e(E_e)$ :

$$k_{e0}^\lambda = \int_0^{\infty} v_{elec} f_e(E_e) \sigma_{e0}^\lambda(E_e) dE_e \quad (32)$$

$$v_{elec} = \sqrt{\frac{2E_e}{m_e}} \quad (33)$$

$$f_e(E_e) = 2 \sqrt{\frac{E_e}{\pi}} \left( \frac{1}{k_{B,2} T_{e,1}} \right)^{\frac{3}{2}} e^{\left( \frac{-E_e}{k_{B,2} T_{e,1}} \right)} \quad (34)$$

Equations 33 and 34 are substituted into Eq. 32 to obtain Eq. 35.

$$k_{e0}^\lambda = \int_0^{\infty} 2E_e \sqrt{\frac{2}{\pi(k_{B,2} T_{e,1})^3 m_e}} e^{\frac{-E_e}{k_{B,2} T_{e,1}}} \sigma_{e0}^\lambda(E_e) dE_e \quad (35)$$

$$k_1^\lambda \approx \sigma_1^\lambda(eV) \sqrt{\frac{2eV}{m_A}} \quad (36)$$

$$k_2^\lambda \approx \sigma_2^\lambda (2eV) \sqrt{\frac{4eV}{m_A}} \quad (37)$$

The cross section areas were retrieved from Y. Chiu et al [15]. With the assumption of quasi-neutrality, the equations can be further consolidated with the following definitions:

$$N_e = N_1 + 2N_2 \quad (38)$$

$$\alpha = \frac{N_1}{N_e} \quad (39)$$

Leaving:

$$I_\lambda = \frac{hc}{4\pi\lambda} N_0 N_e \left( k_{e0}^\lambda + \alpha k_1^\lambda + \frac{1-\alpha}{2} k_2^\lambda \right) \quad (40)$$

Where  $\alpha$ ,  $N_e$ ,  $N_1$ , and  $N_2$  are the ratio of the number of singly ionized atoms to electrons, the number of electrons, the number of singly ionized atoms, and the number of doubly ionized atoms respectively.

However, it was found by G. F. Karabadzhak et al that metastable levels needed to be accounted for to properly reflect the line intensities [14]. The following ratio is defined, which compares the excitation of a metastable level which would impact line intensities from all of the lines of interest that can impact the associated state to one line that can impact the state:

$$K^\lambda(T_e, \alpha) = \frac{\sum_i \left( k_{e0}^i + \alpha k_1^i + \frac{1-\alpha}{2} k_2^i \right)}{k_{e0}^\lambda + \alpha k_1^\lambda + \frac{1-\alpha}{2} k_2^\lambda} \quad (41)$$

The sum above is for the following wavelengths: 823.3 nm, 840.9 nm, 881.9 nm, 904.5 nm, 980.0 nm [14]. The fractional increase in brightness due to these metastable levels is then added to the overall brightness calculation:

$$I_\lambda = \frac{hc}{4\pi\lambda} N_0 N_e \left( k_{e0}^\lambda + \alpha k_1^\lambda + \frac{1-\alpha}{2} k_2^\lambda \right) \left[ 1 + \frac{K^\lambda(T_e, \alpha)}{\zeta^\lambda} \right] \quad (42)$$

Where  $\zeta^\lambda$  was retrieved from G. F. Karabadzhak et al and is only determined by the wavelength of interest. Dividing an equation for intensity of one wavelength by the equation for a different wavelength, a ratio that is only dependent on electron temperature, once  $\alpha$  is set, is the result. The ratio  $\alpha$  typically varies within the range of 0.7-0.95 depending on the specifics of the thruster and its operating conditions [14]. Here  $\alpha$  was assumed to be 0.75, though the ratio only changes minutely to alterations in  $\alpha$ , meaning the choice of what to set it to is of minimal importance for this application. Below in Fig. 2 & 3 are an example curves generated via these calculations.

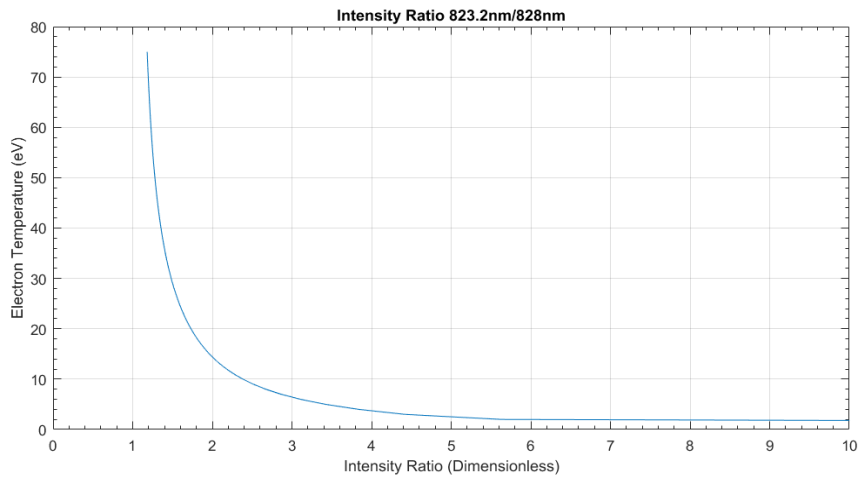


**Fig. 2 Intensity Ratio vs. Electron Temperature.**

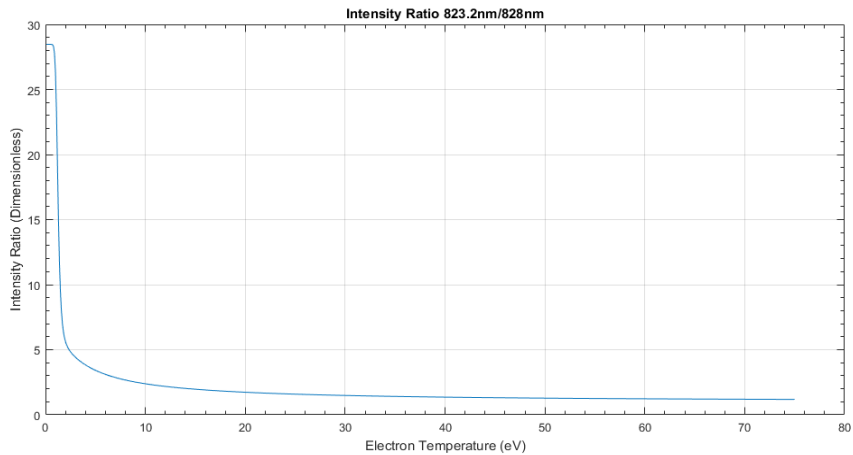


**Fig. 3 Intensity Ratio vs. Electron Temperature.**

However, for use as a diagnostic, a couple of additional criterion must be met beyond soundness of model, though these are more subjective. The generated curve from a ratio must have sufficient slope to be sensitive in the eV range of interest. The raw intensities must be sufficiently bright so that noise is not dominant. As such the 823.2 nm, 828.0 nm, and 881.9 nm lines were selected for use in analysis once all data was collected. Please note that the emission cross sections above 70 eV used in the creation of the model was not empirical in nature, but derived from methods outlined in G. F. Karabadzak et al [14]; as such, above 70 eV the model utilized is subject to greater uncertainty.

### 2.3 Bulk Velocity Drift Correction

Electron movement close to the exit plane of a hall thruster can be rather complex thanks to the present electric and magnetic fields. A hall thruster does not have simple motion of electrons in its active channels either, motion is rather complex in this area. One of the effects of this is a bulk drift velocity. Assuming this drift velocity is entirely in a singular direction in a coordinate system, this can be accounted for by changing the energy distribution used in Eq. 35 from a pure Maxwellian to one with a velocity shift, which was shown to better capture the electron energy distribution functions in the channels of a Hall thruster [16]. Starting with the equation for  $k_{e0}^\lambda$ :

$$k_{e0}^\lambda = \int_0^{\infty} v_{elec} f_e(E_e) \sigma_{e0}^\lambda(E_e) dE_e \quad (43)$$

It can be noted the equation for the electron energy distribution is fully separable. Due to this a new electron energy distribution can be derived and directly substituted into Eq. 43 to arrive at a new function. We begin by starting with the Maxwellian distribution for a velocity vector in three dimensions:

$$f(v_x, v_y, v_z)dv_x dv_y dv_z = \left(\frac{m}{2\pi k_{B,2} T_{e,1}}\right)^{\frac{3}{2}} e^{\left(\frac{-m(v_x^2 + v_y^2 + v_z^2)}{2k_{B,2} T_{e,1}}\right)} dv_x dv_y dv_z \quad (44)$$

Please note that this is for an arbitrary coordinate system, there is no need for this to line up with a natural coordinate system for the thruster, and is simply used as a means of deriving the proper equation. From here a change in velocity in a single direction is introduced for the bulk drift:

$$f(v_x, v_y, v_z)dv_x dv_y dv_z = \left(\frac{m}{2\pi k_{B,2} T_{e,1}}\right)^{\frac{3}{2}} e^{\left(\frac{-m(v_x^2 + v_y^2 + (v_z + \Delta v)^2)}{2k_{B,2} T_{e,1}}\right)} dv_x dv_y dv_z \quad (45)$$

Next the equation is converted to spherical units as we are dealing with a system in which angular positioning is a more natural description of potential movement. While cylindrical coordinates would be more intuitive for our system, due to the axisymmetric nature of the thruster, integration in spherical coordinates is ultimately easier to resolve while ultimately ending up equivalent for the purposes of this diagnostic:

$$f(U)U^2 \sin(\theta) dU d\theta d\varphi = \left(\frac{m}{2\pi k_{B,2} T_{e,1}}\right)^{\frac{3}{2}} e^{\left(\frac{-m(U^2 + 2U \cos(\theta) \Delta v + \Delta v^2)}{2k_{B,2} T_{e,1}}\right)} U^2 \sin(\theta) dU d\theta d\varphi \quad (46)$$

The  $\sin(\theta)$  is left in place and not cancelled out to avoid required use of a modified Bessel function in the integration. From here the function is integrated across all angles to create the following:

$$f(U) dU 2\pi = \frac{2k_{B,2} T_{e,1} 2\pi}{U 2\Delta v m} \left(\frac{m}{2\pi k_{B,2} T_{e,1}}\right)^{\frac{3}{2}} \left( e^{\left(\frac{-m(U^2 + 2U \Delta v + \Delta v^2)}{2k_{B,2} T_{e,1}}\right)} e^{\left(\frac{m(2U \Delta v)}{k_{B,2} T_{e,1}}\right)} - e^{\left(\frac{-m(U^2 + 2U \Delta v + \Delta v^2)}{2k_{B,2} T_{e,1}}\right)} \right) dU \quad (47)$$

After some simplification and rearrangement:

$$f(U) U dU = \frac{1}{\Delta v 2\pi} \sqrt{\frac{m}{2\pi k_{B,2} T_{e,1}}} e^{\left(\frac{-m(U^2 + \Delta v^2)}{2k_{B,2} T_{e,1}}\right)} \left( e^{\left(\frac{m(U \Delta v)}{k_{B,2} T_{e,1}}\right)} - e^{\left(\frac{-m(U \Delta v)}{k_{B,2} T_{e,1}}\right)} \right) dU \quad (48)$$

Recognizing that the last term is a sinh function:

$$f(U)UdU = \frac{1}{\Delta v\pi} \sqrt{\frac{m}{2\pi k_{B,2}T_{e,1}}} e^{\left(\frac{-m(U^2+\Delta v^2)}{2k_{B,2}T_{e,1}}\right)} \sinh\left(\frac{m(U\Delta v)}{k_{B,2}T_{e,1}}\right) dU \quad (49)$$

Defining kinetic energy and change in kinetic energy along with a change in variable to accommodate the function in terms of  $dE$  in the later integral:

$$E = \frac{1}{2}mU^2 \quad (50)$$

$$\Delta E = \frac{1}{2}m\Delta v^2 \quad (51)$$

$$dE = mUdU \quad (52)$$

$$f(E_e)dE = \frac{m}{2\pi} \sqrt{\frac{1}{\pi k_{B,2}T_{e,1}\Delta E_e}} e^{\left(\frac{-(E+\Delta E)}{k_{B,2}T_{e,1}}\right)} \sinh\left(2\frac{\sqrt{E_e\Delta E_e}}{k_{B,2}T_{e,1}}\right) dE \quad (53)$$

The function is then renormalized so that the total integration is 1:

$$f_e(E_e)dE = \sqrt{\frac{1}{\pi k_{B,2}T_{e,1}\Delta E_e}} e^{\frac{-(E_e+\Delta E_e)}{k_{B,2}T_{e,1}}} \sinh\left(2\frac{\sqrt{E_e\Delta E_e}}{k_{B,2}T_{e,1}}\right) dE \quad (54)$$

Then recognizing that the item of interest is the movement of electrons, the following can be assigned:

$$v_{elec} = \sqrt{\frac{2E_e}{m_e}} \quad (55)$$

Equations 54 and 55 are substituted into Eq. 43, resulting in Eq. 56.

$$k_{e0}^\lambda = \int_0^\infty \sqrt{\frac{2E_e}{\pi k_{B,2}T_{e,1}\Delta E_e m_e}} e^{\frac{-(E_e+\Delta E_e)}{k_{B,2}T_{e,1}}} \sinh\left(2\frac{\sqrt{E_e\Delta E_e}}{k_{B,2}T_{e,1}}\right) \sigma_{e0}^\lambda(E_e) dE_e \quad (56)$$

Finally, the contribution of bulk drift velocity is calculated and substituted in:

$$\Delta E_e = 0.5m_{e,2}v_{elec,d}^2 C_{J to eV} \quad (57)$$

$$v_{elec,d} = \frac{E_{field}B}{B^2} \quad (58)$$

This is then propagated back through the other equations presented above in the collisional radiative model section. Please note that for this analysis, the ExB drift velocity is assumed to

be constant throughout the area of investigation presented in this paper. While this is an incorrect assumption, it allows for a simpler initial estimate analysis as the shape of the E and B-field does not need to be known.

The following is the function if a modified Bessel function of the first kind is acceptable, though it was not used in this study, and has not been normalized:

$$f(E_e)dE = \pi \left( \frac{m}{2\pi k_{B,2} T_{e,1}} \right)^{\frac{3}{2}} e^{\frac{-(E_e + \Delta E_e)}{k_{B,2} T_{e,1}}} I_0 \left( \frac{2\sqrt{E_e \Delta E_e}}{k_{B,2} T_{e,1}} \right) dE \quad (59)$$

The figure below, Fig. 4, is a plot of several different possible electron energy distributions, including the one derived in this paper. The plots are from a study that included an analysis of the best fit for the electron energy distribution in the channels of a Hall thruster. In this investigation it was found that a Maxwellian with a velocity shift, such as derived above, was the best fit in its area of investigation. The other distributions are presented as well for examples of how the shape of the electron energy distribution function could alter based on different assumptions.

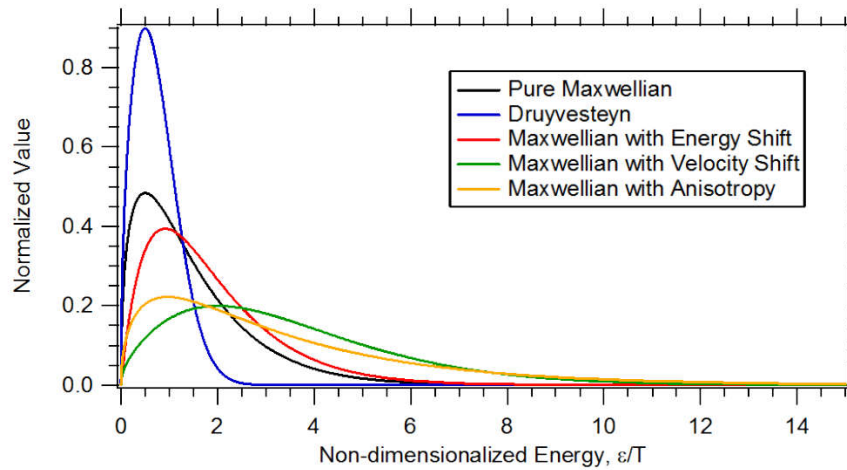


**Fig. 4 Energy Distributions [16]**



## 2.4 Abel Inversion

One major hurdle is the fact that since spectrometer readings will be a sight-line integral of the intensity at each individual point, we cannot directly use the readings from the spectrometer. However, due to the nature of a Hall thruster, the plume has a light intensity profile that can reasonably be modeled as axisymmetric, and from our model we have predictions for line intensity. In addition, the sight line intensity is a line integration of all points along said line, where the equation for this would be:

$$I_{\lambda}(y) = 2 \int_y^R I_{\lambda}(r) \frac{r}{\sqrt{r^2 - y^2}} dr \quad (60)$$

Where  $r$  is the radial coordinate and  $y$  is the linear coordinate from the centerline of the thruster along the plane parallel to the thruster face. Thanks to these facts, the electron temperature of a point in a plume can be determined by analysis of the Abel inversion of the emission intensity of a sight line through the plume, where the equation for the Abel inversion itself is:

$$I_{\lambda}(r) = -\frac{1}{\pi} \int_r^R \frac{d(I_{\lambda}(y))}{dy} \frac{dy}{\sqrt{y^2 - r^2}} \quad (61)$$

However, since data are obtained in discrete points as supposed to a continuous function, it is not possible to use this equation directly. Furthermore, the above Abel inversion assumes that a function with no discontinuities exists to describe the intensity, which may not be the case for empirically collected data. Instead, two techniques were used: h-interpolation and Fourier based fitting. Each is a different means to apply an Abel inversion to discrete data. The Abel inversion for functions with discontinuities is not presented due to not being used in this study and converges to the standard Abel inversion when no discontinuities are present.

### 2.4.1 h-interpolation

h-interpolation involves the creation of the needed derivative for the Abel inversion by use of linear, higher order, smoothing spline, or other fit of the points to create a differentiable function. From this a derivative is calculated and used in the integral for the Abel inversion. This study uses a cubic smoothing spline with the smoothing parameter automatically generated by the analysis software for h-interpolation. Due to standard and widespread use of a smoothing spline fit in data analysis, derivation is omitted for brevity.

### 2.4.2 Fourier Method

The Fourier based method works via assuming the radial distribution is a cosine series expansion [17]:

$$I_{\lambda}(r) = \sum_{n=N_l}^{N_u} A_n I_{\lambda,n}(r) \quad (62)$$

$$I_{\lambda,0}(r) = 1 \quad (63)$$

$$I_{\lambda,n}(r) = 1 - (-1)^n \cos\left(n\pi \frac{r}{R}\right) \quad (64)$$

Thus the sight line integral of the point intensity along a sight line would be:

$$I_{\lambda,fit}(y) = 2 \sum_{n=N_l}^{N_u} A_n \int_y^R I_{\lambda,n}(r) \frac{r}{\sqrt{r^2 - y^2}} dr \quad (65)$$

While the  $A_n$  are still not known, the fact that this needs to fit the experimentally gathered data allows us to use least squares analysis to find best fits for  $A_n$ . From here the  $A_n$  are then substituted back into Eq. 62 to produce our radial intensity function.

One of the major benefits of this method, is that it can be used as a band pass filter. This is due to the fact that the number of terms selects the number of frequencies that the

process is effectively considering. This feature is rather useful for the purposes of filtering out noise. The downside to this is that the number of terms must be selected by the person doing the analysis. Due to this there is some uncertainty introduced associated with the number of terms used, though it is extremely hard to estimate the exact amount of error introduced. One means of ascertaining the proper number of terms to use is to compare the resultant function from the Fourier method with a different methodology. While this means that some behavior might be potentially missed, it does ensure a higher level of self-consistency between the methods. In this context, an inability for the two methods to agree on general shape regardless of number of terms is indicative of an area in need of additional consideration. This consideration must be nuanced, since care must be taken that unexamined assumptions are not feeding into the judgement regarding whether disagreement is due to actual process sensitivity and other meaningful causes, or idiosyncrasies of the analysis method, data collection, and other minutia that produce unexpected results.

## CHAPTER III

### EXPERIMENTAL FACILITY

#### 3.1 Thruster Setup

The experiment took place during a number of experimental runs of the Technology Development Unit for HERMeS (Hall Effect Thruster with Magnetic Shielding) Three Hall thruster in Vacuum Facility 5 in building 301 at NASA Glenn Research Center, pictured in Fig. 5. VF-5 is a large-scale vacuum chamber that is capable of pump down to pressures sufficient to test space-based equipment. This is primarily utilized to test electrical propulsion devices. Gathering data for this experiment was one of many tests conducted during this run

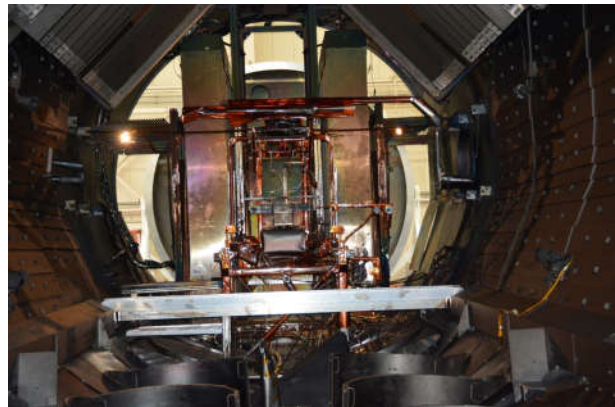


**Fig. 5 Thrust Stand Setup**

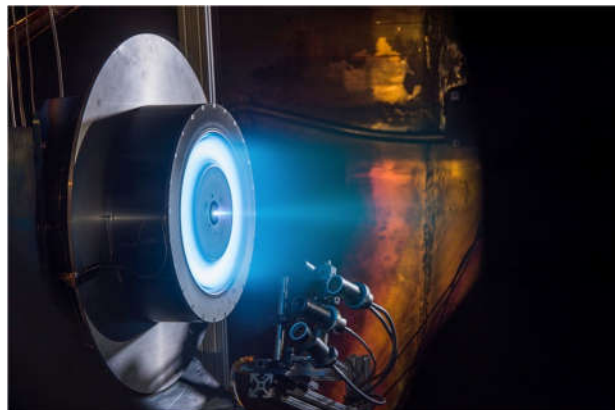


**Fig. 6 Operating Hall Thruster [25]**

which was centered on understanding wear characteristics to allow for better modeling and extend the expected operational life of the device.

The hall thruster itself was attached to a thrust stand and connected to general support items, such as the power supply and propellant lines, to allow for its operation in the chamber. Notably, the thruster body is electrically tied to the cathode potential while still receiving power, fuel, and instrumentation communication from outside the vacuum chamber. Once testing operations began, the chamber was pumped down to roughly  $10^{-8}$  torr. At this point xenon was then fed to the thruster, its magnetics engaged, and systems brought to voltage. Figure 6 provides an example of a thruster in normal operation for illustrative purposes.

### 3.2 Thrust Stand

The thruster itself was mounted onto a null-type inverted pendulum thrust stand for the purposes of measuring thrust, which was of importance to other tests that were ongoing. Please see Ref [18] for the details of the theory behind such a device. This stand allowed for the thruster to remain stationary during operation, and adjust the inclination of the thruster via use of a stepper motor. [5, 19]

### 3.3 Vacuum Chamber

As mentioned, Vacuum Facility 5 is a vacuum chamber in NASA Glenn Building 301. The chamber is approximately 4.6m in diameter, and 18.3m long. Cryopanelts were used to evacuate the chamber down to the required pressures for a test. For the duration of the testing that occurred chamber pressure was monitored using three xenon and one air calibrated ion gauges. [5, 19]

### 3.4 Power-Supply and Control Systems

The thruster was controlled by power racks which had the power supplies for the discharge, inner and outer electromagnet, cathode heater, and cathode keeper. Discharge power consisted

of three 15 kW (1000V 15A) power supplies in a master-slave configuration. A computer monitored the voltages, currents, temperatures, flow rates, pressures, and thrust of the thruster via a multiplex datalogger. [5, 19]

### 3.5 Flow System

A laboratory grade feed system was utilized in the operation of the Hall thruster. This system was used to feed xenon to the thruster itself as well as elevate background pressure, and consisted of four mass flow controller (MFC). Xenon was used provided to the thruster and cathode using 500 sccm and 100 sccm MFCs. [5, 19]

### 3.6 TDU-3

The specific Hall thruster involved was the Technology Development Unit 3, a development unit for the HERMeS program. It utilizes magnetically shielded channels with boron-nitride-silica composite wall material to ensure long life of the thruster [4]. Its intended operational point is at 300-600V, 20.8A, and the HERMeS specifications calls for ability to operate at a low power condition, 300V 9A [5]. Full details and comparisons to TDU-1 and 2 can be found in Kamhawi et. al [4].

### 3.7 Instrumentation System

An optical collection assembly with an attached collimator was placed on a linear movement stage with two degrees of freedom, allowing for movement up/downstream and adjustment of its place in the edge on profile. This allowed for a wide range of points to have data be collected from. The purpose of the collimator was to reduce the amount of extraneous light that is passed to the

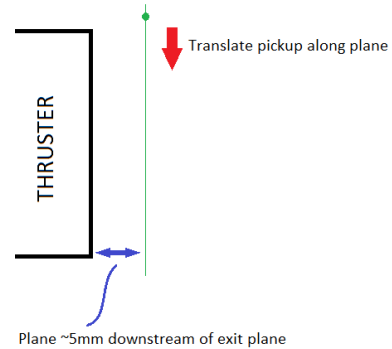


**Fig. 7 Data Collection Plane**

optical pickup itself. Without a collimator, the emission from the entirety of the probe could contribute to the readings, instead of emission only along a sight line.

The light from the collection assembly was routed to a StellarNet BLACK-Comet-SR, a spectrometer, via fiberoptic cable to determine the line strengths. The StellarNet BLACK-Comet-SR is capable of wide range spectra reading, specifically it is rated for a 880nm range. Power is provided by USB, and it is capable of integration times from 1ms to 65s. This spectrometer was connected to a computer that was capable of reading, storing, and displaying the spectral data.

### 3.8 Calibration and Alignment

Prior to closing and pumping down of vacuum chamber, the optical pickup was installed in said chamber and alignment was performed. This consisted of shining a low-power red, 632 nm laser through the installed fiber optic cable to exit the collection end. This allowed for visual alignment and determination of the exit plane of the thruster with regards to the motion stages and ensuring that the collection sight-line was parallel to the exit plane.

The software was configured to take readings that were an average of two scans of four seconds each. This was to help even out the inherent noise in short collection times and provide enough gain to ensure proper distinction between low intensity values. In addition, the software was used to properly zero the collection of the spectrometer setup so that only the emission from the plume would be counted towards intensity.

Calibration of the optics train consisted of placing a standard xenon lamp at the same distance as data collection. Spectral data was recorded through the collection optics and entirety of data collection system. This gave the transmission characteristics of the system which were taken into account with regards to data analysis. When repeated testing of the same operating conditions occurred, spectra were recorded. This showed no significant changes in intensity.



## **CHAPTER IV**

### **DESCRIPTION OF EXPERIMENT**

Data collection took place during the operation of the wear testing campaign for the TDU-3 that was underway at NASA Glenn. Due to the nature of the opportunity to collect data, operational conditions of the thruster were dictated by the wear campaign and were not decided or influenced by this study. As such, only a limited number of operational conditions had data collection for this study, though the technique should be applicable to any other operating condition that is intended use for the thruster. The only restriction that is absolute is that a full sight line across the plume must be possible for any downstream distance that data is desired to be collected at. If this is not possible, Abel inversion cannot be performed.

Operations started once the chamber was brought to proper pressure. At this point, the thruster was run at a series of specific parameters to ensure that proper thermal conditions had been met on the device itself, and also address the fact that component parts had been exposed to normal atmosphere, thus lingering elements could still be present in the device unless a bake out period was performed. In addition, this period served as an additional check to see that everything was properly functioning. Unexpected hotspots, plume fluctuations, or other unintended behavior could be caught in early stages so that a call between cancelling data collection or assuming risk from unusual behavior was not as difficult of a decision.

Once the thruster had been brought to the operating condition to be used for the wear test, enough time was allowed to pass to allow for the thruster to settle into equilibrium at this set of parameters. Then the optical pickup was set to begin taking data points at the plane of interest closest to the Hall thruster. At a set of evenly spaced points, data was collected, with time allotted to allow for any vibration caused by the movement of the data collection apparatus to settle. The length of the linear motion stage was such that points could be taken from outside the outer edge of one side of the plume, to outside the outer edge of the other side of the plume. Once all data in this plane had been collected, the linear motion stage allowing for up and downstream motion was engaged, and data was collected in a new plane.

While the spectrometers were capable of capturing intensity information for a broad spectrum, only intensities of lines of interest were recorded. This was accomplished via software filtering of the raw feed. The spectrometers were set to take readings that were the average of two samples, each with four seconds of integration time. The purpose of this was to reduce the potential for noise that might cause the data points to be skewed from a true representative value, which if not addressed could prevent proper analysis. This averaging and duration was chosen as a compromise between maximizing signal to noise and required measurement time. The lines that were recorded were all within the sensitivity range of a single model of spectrometer, so no error due to different spectrometers capturing different lines was introduced.

#### 4.1 Residuals and Electron Temperature Calculation

Once data had been collected, the intensities were normalized with the data point recorded furthest from the radial center of the plume being treated as the zero intensity before performing the Abel inversion. This is due to the fact that the inversion technique requires the

end value to be zero as part of its boundary conditions. Electron temperatures were calculated by minimizing the relative average least squares of the two-line ratios used at each data point: 823.2/828 and 881.9/828:

$$Residual = \frac{1}{n} \sum_{i=1}^n \frac{(Ratio_{rec} - Ratio_{fit})^2}{Ratio_{rec}^2} \quad (66)$$

Where n is the number of ratios used, both attempted fit and recorded are the same ratio for a given set, and the residual is changed only by changing the eV input to the equation that determines and creates the fit ratios. The equations for the ratios themselves are generated via the equations discussed in the collisional-radiative model section. The reduction of the residual in this manner is equivalent to a maximum likelihood estimation where the fitted value is the mean and the observed value is the variance. To show this, we begin with the normal probability distribution, which we wish to maximize:

$$f = \frac{1}{\sqrt{2\pi\sigma^2}} e^{-\frac{(x-\mu)^2}{2\sigma^2}} \quad (67)$$

However, since probability is always positive, it is possible to maximize the log of the function instead:

$$\log(f) = -\log(\sqrt{2\pi}) - \log(\sigma) - \frac{(x - \mu)^2}{2\sigma^2} \quad (68)$$

Due to the fact that only the terms with the mean are dependent on the model, all terms that do not have the mean in them may be dropped for the purposes of maximization, leaving:

$$-\frac{(x - \mu)^2}{2\sigma^2} \quad (69)$$

However, maximizing this function is the equivalent of minimizing the following due to being the argument of an exponential function:

$$\frac{(x - \mu)^2}{\sigma^2} \quad (70)$$

Where the two is dropped due to being a constant. As may be noted, this is the same as a single term of the residual if the mean is the predicted value, and the observed value is the variance. Furthermore, since the probability of A and B is A times B, the equation for maximizing the probability of all estimates is multiplication of all probability functions together. Thanks to the properties of exponentials, this simplifies to:

$$f = \left( \frac{1}{\sqrt{2\pi\sigma^2}} \right)^n e^{\frac{-\sum_{i=1}^n (x_i - \mu)^2}{2\sigma^2}} \quad (71)$$

And again, taking the natural log of the equation, reducing to only terms that may be maximized, leaves:

$$\frac{-\sum_{i=1}^n (x_i - \mu)^2}{2\sigma^2} \quad (72)$$

Which is again, the same as minimizing its negative. It may also be noted that due to constants not being important for the purposes of optimization, is the same as minimizing:

$$\frac{1}{n} \sum_{i=1}^n \frac{(x_i - \mu)^2}{\sigma^2} \quad (73)$$

This happens to be the same as our residual calculation, thus minimizing residuals is the same as a maximum likelihood estimator if the predicted value is the mean, and the observed value is the variance.

More line ratios would improve accuracy, but in this study, only two were used due to the selected ratios having the best characteristics with the data collection setup used.

## 4.2 Data Processing

Data processing post collection was performed with MATLAB with custom coding. This code was designed to take all raw data for a test at a single time in the form of a multidimensional matrix that assumes even spacing along the coordinate direction required to produce the Abel inversion, though spacing in the x and y direction need not be the same. The advantage of this approach is that the analysis can be adapted to any form of data collection that produces evenly spaced data points along the axis of interest, such as filtered photographs for example. The downside is that the data must be evenly spaced across the plume.

The code starts by taking the raw data, normalizing to the end values, then performing an Abel inversion to find the point intensities of each wavelength. This is done for both techniques of Abel inversion before proceeding to the next step. These intensities are then used to calculate the intensity ratios, which are used in the residual calculation described above. Residual calculation is modular, such that additional ratios may be added with comparative ease. The resultant electron temperatures and residuals are stored for later use and analysis.

The calculation of residuals is rather intensive if simplification measures are not taken. For example, once the E and B fields are known, approximate equations for intensity ratios versus electron temperature may be generated via curve fitting of input and output of the original equations. This would consist of running the calculations for a wide range of electron temperatures, then creating a fitted line equation for the inverse. From this a fast means of determining the electron temperature from the line intensity ratio would be available. The creation of these equations is unfortunately also calculation intensive; however, it may be performed during data collection or preparation for the experiment proper if the values of the fields are known ahead of time, thus allowing for parallel work flow. Each additional line ratio used for analysis increases the amount of computation required for the residuals by a

substantial amount, and as such it is highly recommended that this simplification is used if possible. However, the results presented in this study did not have this simplification performed, as code verification and flexibility were prioritized over runtime optimization.

## **CHAPTER V**

### **RESULTS AND DISCUSSION**

Please note that on all charts the center of the channel in the Hall thruster is at  $3/4 R$ , starts at  $1/2 R$ , and end at  $R$ . Please note that this does not mean the outer diameter of the overall thruster ends at  $R$ , the outer edge of the channel was simply chosen as  $R$  for convenience and hope that channel edge would be of more utility than the outer edge of the casing. It is also important to keep in mind that  $R$  does not correspond to the edge of the plume, especially the further downstream the dataset.

The Abel inversion used to extract the required point intensities was performed with, where possible, both a Fourier method and an h-interpolation method. Fortunately, no discontinuities needed to be assumed to resolve the presented data, though there were some data sets, namely those closest to the thruster, that were too ill behaved to produce any sensible result. Initial assessments indicate that the electron temperature in this area is too high for the techniques used to be reliable. As such, they will not be presented.

Also of note is the fact that not all data presented extends to the same radial distance from the centerline of the thruster. This is not due to a difference in data collection, but rather the result of a noise dominated region of the data. The plasma at enough of a distance from the channels close to the thruster is thin enough to the point that it is difficult or impossible to

get a reliable reading on the brightness intensity. At these points it begins to become debatable whether the plasma is still present, or if readings are nothing more than erroneous readings caused by less than fully ideal equipment and perfect setup.

### 5.1 300V 75%B

Presented below is the result of the lines for the operating conditions of 300V 75%B at 21A. The missing point in the Fourier based analysis closest to the exit plane in Fig. 8 is due to the reported electron temperature dropping below the validity range of the equations in use. Interestingly the electron temperature appears to be highest at a point that is further away from the exist plane rather than the closest points in Fig. 8. Possibly the configuration of the fields could be encouraging the grouping of higher energy electrons in a narrow band. It is also possible this is simply some experimental error, or a reflection of some form of time dependent behavior. Despite that fact, the electron temperatures at that distance are still the lowest on average of the entire set. There is a general tendency of the highest temperatures to be centered around the approximate center of the channel as well in both Fig. 8 & 9, though Fig. 9 shows a much less smooth set of results. This is generally the expectation of h-interpolation, as it does not have the capacity to filter noise in the manner that the Fourier method is capable of. The behavior of a data-set that was collected at a distance of 1mm downstream did not produce useful results, and thus is not presented here. Intensity ratios were such that they were predicting temperatures extremely outside the validity of the models and/or appeared to be fraught with discontinuities. While it might be possible to extract relevant information from this set of data, declarations of discontinuities must be made. Thanks to the fact that it is unclear if the discontinuities are real, or the result of a lack of precision, and the large effect of a discontinuity declaration this study refrains from any such attempts.



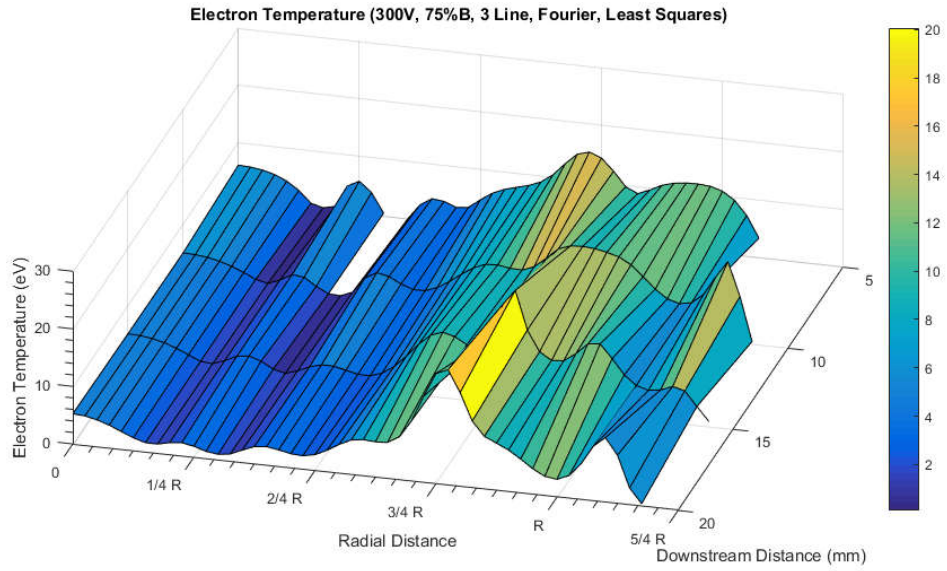


**Fig. 8 Electron Temperature 300V 75%B, 3 Line, Fourier**

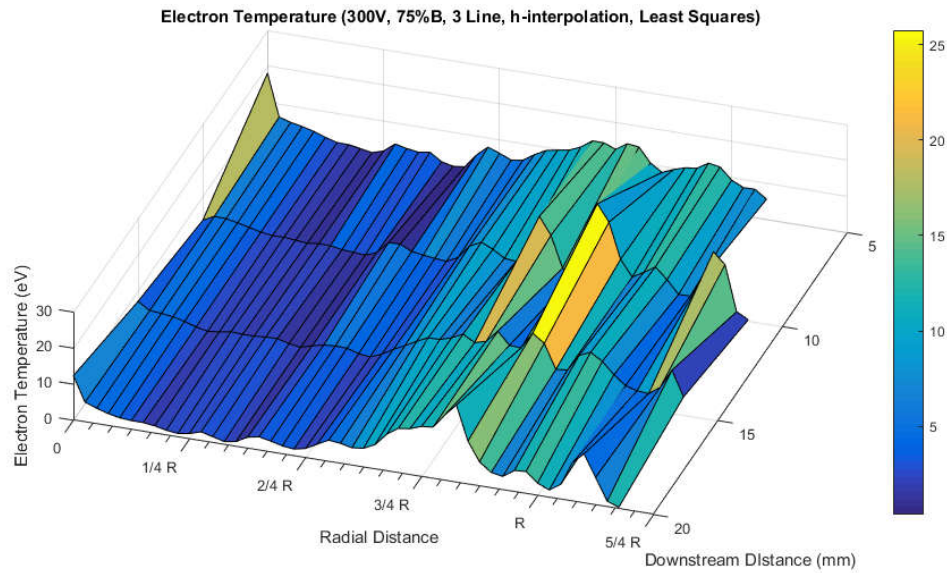


**Fig. 9 Electron Temperature 300V 75%B, 3 Line, h-interpolation**

## 5.2 300V 125%B

Figures 10 & 11 show the reconstructed electron profile generated from the data for 300V 125%B 21A operation. As generally expected, there is a peak of electron temperature at roughly the center of the channel. This is most prominent closest to the thruster but becomes

less extreme as downstream distance from the exit plane increases. On average electron temperature drops the further away from the exit plane, which is what would be expected for this sort of device. As can be seen in Fig. 11 there appears to be some form of behavior that results in a large temperature peak near the centerline of the thruster at 10mm from the exit plane. Most likely this is a non-physical result, and instead is probably due to a high frequency behavior that was filtered out by the Fourier method.

Similar to the 300V 75%B case, there was a set of data collected at 1mm downstream from the exit plane. Also similar to the previous case, the generated results were not sensible, again due to intensity ratios ending up outside of the validity range of the model being employed. The behavior indicating potential discontinuities was present as well, though this in the opinion of the author is more indicative that closer spaced data points are required. This of course is a limitation of the equipment and setup, since proper resolution is required to be able to observe fine detail. Again, the h-interpolation method seems to be responding to some form of behavior too fine for it to discern, but is unable to filter.

Finally, the large spike in temperature near the exit plane is from a region of intensity ratios that are rather sensitive to noise. This large temperature is again, likely non-physical, though it is quite reasonable to assume that it is indicative of an area of higher temperature if not as large as indicated. Simply one that further refinements of the technique would be needed to resolve with any true degree of confidence, and most likely not to the extreme seen in the charts.

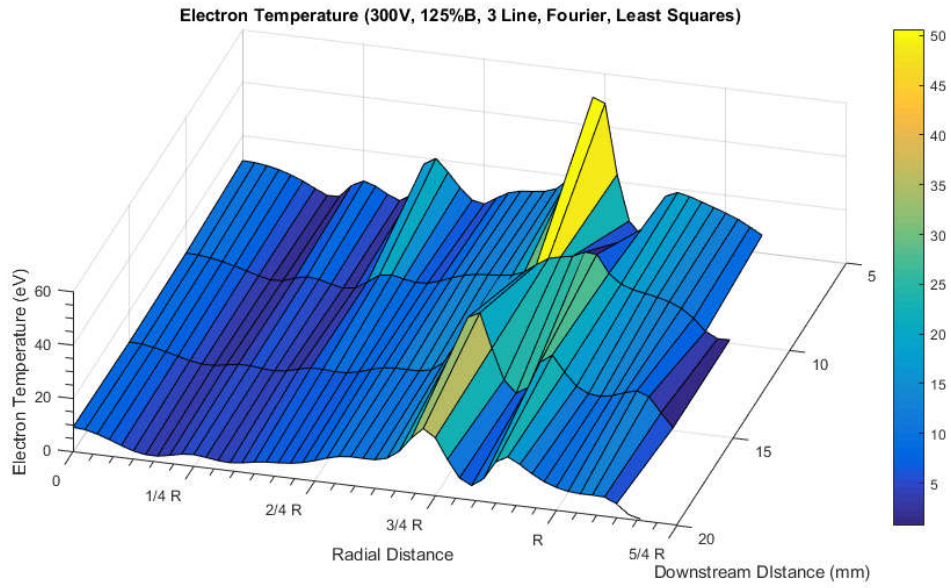


**Fig. 10 Electron Temperature 300V 125%B, 3 Line, Fourier**

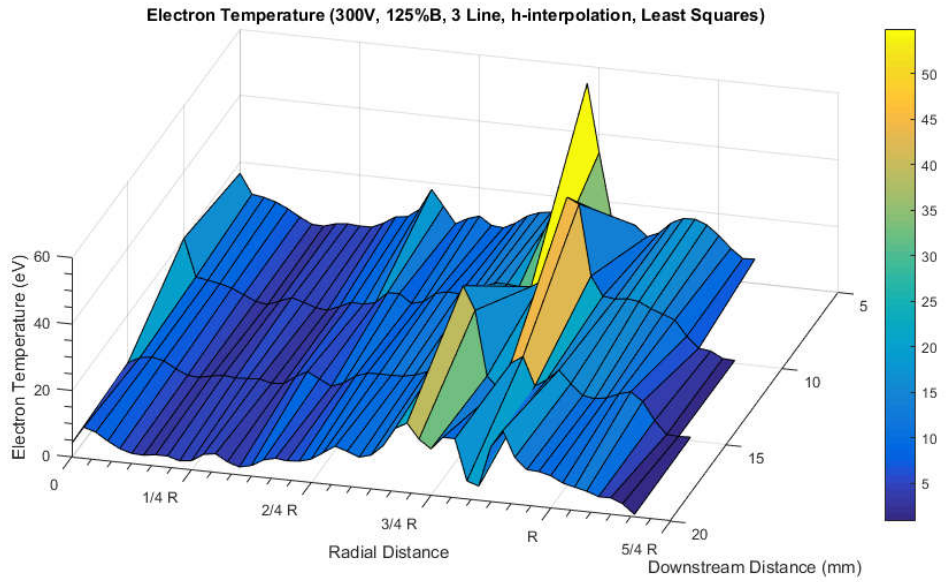


**Fig. 11 Electron Temperature 300V 125%B, 3 Line, h-interpolation**

### 5.3 Comparable Data

Presented below is similar data to compare gathered results to. Unfortunately, they are not direct 1:1 comparisons, as they are from a different thruster, with the exception of Fig. 15, and different operational parameters.

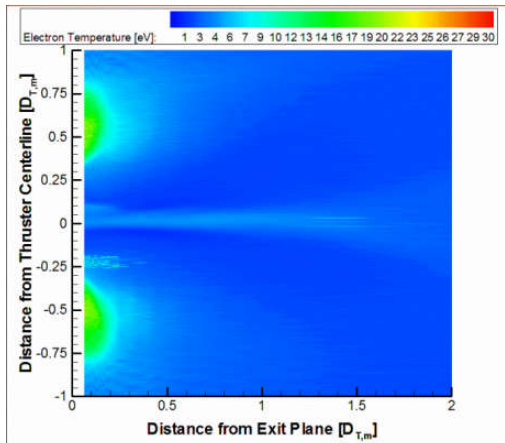


Fig. 12 Comparison Data, 300V 30kW [20].

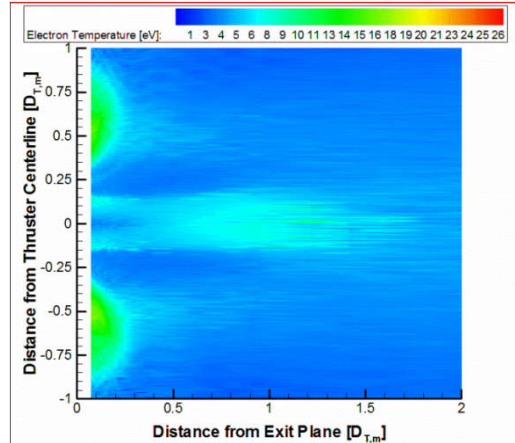


Fig. 13 Comparison Data, 300V 10 kW [3].

Figures 12 and 13 show electron temperature data from operation of the NASA-457Mv2 Hall Thruster and the NASA-300M Hall Thruster respectively. Please note that this is a different thruster and different operational point. However, of note is the regions of higher electron temperature centered around the channels of the thruster with higher temperatures reaching further out radially on the outer side compared to the inner side, and the tendency of the electron temperature to drop off downstream.

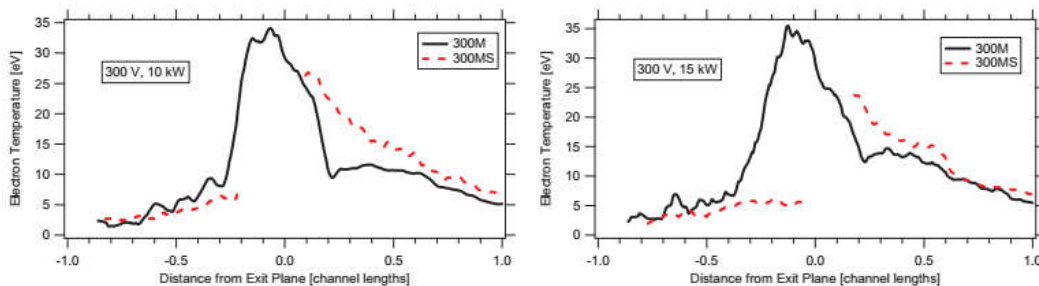
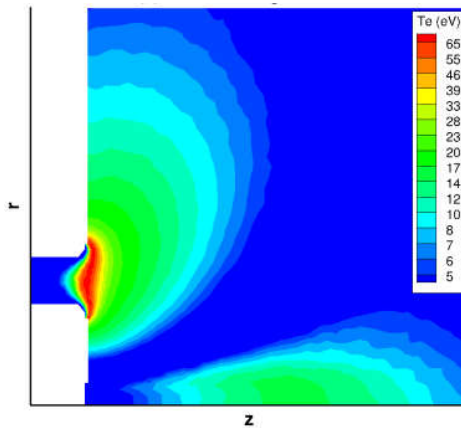


Fig. 14 Comparison Data, 300V 10 kW & 300V 15 kW, Channel Centerline [21].

In Fig. 14, probe data from the centerline of the channel of the NASA-300M and NASA-300MS Hall thrusters is shown. Note that this is not a radial distance profile, but rather data from a single radial distance and a number of downstream distances. Again, this is a different thruster at a different operational point, but will help establish the general trends of expected behavior.



**Fig. 15 Comparison Data (Simulation), 600V 12.5 kW [2]**

The data shown in Fig. 15 is not empirical data. Rather, it is data generated by the computer simulation for the thruster used in this study at the 600V 12.5 kW operating condition generated for studies of thruster wear at NASA Glenn [2]. Again, note the high temperature centered around the centerline, that extends further radially on the outer side as compared to the inner side.

The comparison data suggested that a rise in electron temperature should have been seen at the centerline of the thruster, and a difference was observed. However, it was not as large as Fig. 15 would suggest could potentially be expected. It is quite possible that data collection simply did not extend far enough in the downstream direction to have a chance to note this behavior. Alternatively, it is possible in this configuration of thruster parameters that the expected difference would not be as large as in the 600V 12.5 kW case.

## 5.4 General Observations

### 5.4.1 Data

While most of the plume that was investigated was able to be resolved, there reached a point radially far enough from the plume where the plasma was diffuse enough that noise dominated the readings. In this region, no reliable electron temperature readings could be produced. Fortunately, these areas are not usually of great interest to the operation of the thruster, so the fact that electron temperature could not be resolved is of minimal concern for the intended application. If behavior in this region is of particular interest to a researcher, it is not recommended that this technique is utilized. It is ill-suited to the especially sparse conditions that are present in this area.

On average, the electron temperature of the plume dropped the further away from the exit plane the reading was taken, which is expected behavior. Generally speaking, the expansion of the plume away from a means to re-excite the electrons means that the plasma will tend to settle into less energetic states in accordance with thermodynamic principles as the plasma expands and moves away from the electrons confined in the Hall current. Of interest is the fact that on average the electron temperature of the 75%B case was less than the electron temperature of the 125%B case. This could be explained by the kinetic energy of a given electron being greater due to the increased gyrofrequency at start, as electric field strength was the same in both conditions. That said, the 75% B case was calculated to experience a greater  $E \times B$  drift, which some diagnostics might be more sensitive towards. This is suggestive that high B versus low B might display different behaviors even if high versus low values are fairly close in terms of absolute magnetic field strength. This would be due to the fact that  $E \times B$  drift is affected by both the electric and magnetic field strength. Meanwhile the gyro frequency is mainly a function of the magnetic field strength. While both arise from the Lorentz force, they

exhibit said influence in different ways, therefore given different relative values of the magnetic field to the electrical field, different behavior would be expected. This likely would have consequences on thruster design and life if not properly accounted for, since thruster throttling would have to take into account these effects even outside of the acceleration areas of a thruster. The shifting of the relative ratios of the two may cause concerning behaviors to occur in different locations in the plume or near-field even if the same field shape, merely scaled, is maintained. In some locations this behavior might be less critical to take into account, but in others it may cause greater consequences.

As a suggestion, it seems worthwhile that as extreme a range of the ratios of the electrical and magnetic field strengths be tested to see if any unexpected modes of behavior arise. Unexpected potentially consequential operational behavior may be predisposed to arise even at low power settings potentially. In the event that said undesired is found, it would seem worthwhile to test different strengths while maintaining the same ratio to determine if the concern is more a function of the absolute strength, or the ratio of the strengths.

#### 5.4.2 Diagnostic Implementation

Moving on from observations regarding the data itself, and onto the specifics of the implementation of the diagnostic, calculation time of the electron temperatures is quite long; on the order of several hours on a standard desktop computer for the amount of data collected and presented in this study. If the simplified equations for intensity ratios are not pre-calculated such as was suggested in the data processing section of this paper, it is likely processing will take significant time for any test taking a useful amount of data at more than one downstream distance. Due to this, use of this diagnostic for real-time or quickly calculated snapshot purposes is not feasible if the values and shapes of the electrical and magnetic fields are not

already known. However, if the values are known and the equations can be pre-calculated, analysis time drops significantly, such that the limiting factor for fast display of electron temperature is data to the end user is collection rate when a moving collection head setup is used.

If this hurdle can be overcome, the path is open for development of near real time analysis provided a concentrated effort is made to optimize the calculation and code involved with the technique. Due to the nature of multiple wavelengths being examined at the same time, there is ample possibility to improve speed via the use of parallel computation, which was not utilized at this stage. This is only one example of an opportunity for potential optimization of computation.

It must also be noted that it is important to allow the optical pickup to settle after movement to a new position to prevent introduction of error. Given the distance from the plume itself, even fairly small angular differences can produce a rather large difference in the measured sight-line's path. This can be mitigated by mount design and specifics of the linear movement stage, but implementation of the diagnostic must take this into account.

## 5.5 Diagnostic Utility

To assess the utility of the technique, we must be able to judge its accuracy, ease of deployment, and cost. Cost is the easiest to assess: if one can afford to operate a vacuum chamber for extended periods and provide the needed xenon to a thruster, the setup is affordable and will not take a significant amount of the budget to acquire and set up the needed equipment if not already available. In addition, it is quite easy to justify these costs since the items involved can be easily reused in many different other procedures. One main cost concern that may arise however is if specific custom coding beyond the most basic of implementation



is required, either for integration into other systems, or for troubleshooting should issues arise. Programming costs can be quite high if no one within an organization has the needed knowledge to do such a task in-house.

In regards to how easy it is to deploy, this fortunately is also rather in the technique's favor. A linear movement stage needs to be mounted inside the vacuum chamber that has an optical hookup attached. Provided there are mount points and an optical through port is available, this is a simple enough task. While it is possible to collect data through an optical window, this is not recommended. Corrections must be made for the optical properties of the window, and it is unlikely that travel across the entire diameter of the thruster plume will be readily achievable. The main difficulty is in the analysis of the collected data, provided it is possible to mount collection hardware without optical intermediaries. No standard software exists to perform the analysis so custom code will be required unless the investigator has a prior relationship with an institution that is already conducting such research. This is a comparatively minor hurdle, but it is something to take into consideration if no one with the needed coding knowledge is available. As mentioned previously, coding costs can mount up, though the code involved is simple enough that training an individual within the organization to have on hand is quite feasible.

Accuracy is rather hard to judge fully at the present time. An exact one to one data set collected by other means does not exist to the author's knowledge, and the simulation data for electron temperature being prepared by others for this combination of parameters and thruster is not ready for publication at the time of writing. As such, trend comparison is the most viable option, which is suggestive that overall the technique's resultant electron temperature is agreeing with the other literature's trends [8-11]. The average electron temperature drops in a

manner similar to the data shown in Fig. 12-15. The peaks further downstream from the exit plane in Fig. 8-11 could correspond to the rises seen in Fig. 14. On the other hand, as mentioned in prior sections, the electron temperatures seen at these peaks are in a range in which there is a high level of uncertainty, so they might simply be statistical noise. In addition, in the initial proposal of the collisional radiative model as a potential diagnostic, agreement was tested against probe data [14] and found to agree in lower electron temperatures, even if disagreement was observed in higher electron temperatures due to the Langmuir probes being in a configuration more sensitive to low energy electrons [14].

As previously mentioned, it seems feasible to reduce calculation time of electron temperature to the point that this technique could be used as a runtime diagnostic if proper optimization, data collection methodology, equation pre-calculation, and dedicated computational hardware issues are addressed. This would be of great value to help understand the functioning of a Hall thruster, as it would allow exploration of the electron temperature of the plume during the operation itself, which may provide additional insight into the status of the thruster during testing. The benefits of this would be multiple, it provides a potential means to warn operators that unexpected behavior is occurring, evolution of the plume could be observed with much greater ease, and the provided data might be of utility for optimization of operational conditions for desired performance.

Given the lower levels of uncertainty present in regions of lower electron temperature thanks to the fortunate behavior of the correspondence of intensity ratio and electron temperature, this manner of diagnostic would be a rather excellent fit for locations further downstream as well. The use of multiple diagnostics in a single experiment, the one presented in this study and the use of a Langmuir probe would allow for cross-confirmation of data. A

concordance of agreeing results would do much to increase the confidence in the analysis of the behavior of a given thruster.

Alternatively, one diagnostic could act as a filter for the other to determine regions requiring more intense investigation. Given the particulars of an experiment, this could lead to potential appreciable reduction in required time to gather data of interest if one diagnostic requires significantly different amounts of time. Of course this may not always hold, so the viability of this functionality may vary according to experimental setup.

At the moment, it appears that the technique will provide a cheap and easy to incorporate non-intrusive means to assess the plume, though not in a fashion that is close to real time. While this does mean that there is definitely room for improvement, even at this stage once institutional trust is established for the method it can still provide a means to empirically test models for the steady state situation of a new thruster.

## 5.6 Error Discussion

Based upon Pretzler et al. [22], a tentative worst case estimate of the systemic error of plus or minus twice the value shown in Fig. 16 can be assigned to every data point's intensity ratio from Abel inversion in principle. This is based on the errors seen in their examination of arbitrary

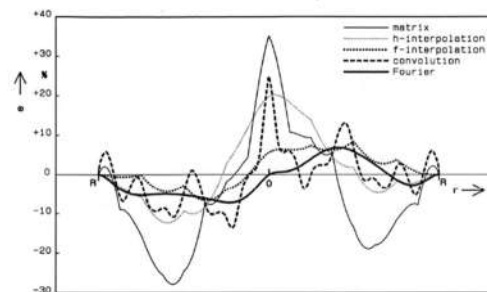


Fig. 16 Single Able Inversion Error [22].

hypothetical data that would be investigated by Abel inversion, and cross confirmed in their results with a controlled experiment. The doubling comes from the propagation of error of two Abel inversions. The greatest error is near the center of the profile for the h-interpolation, and greatest at the middle of the reconstruction for Fourier. It was also noted that having an

undersized radius, compared to the radius of the object of investigation can cause large issues with Abel inversion [22]. This is the main reason data collection continued into the diffuse sections of the plasma that were noise dominated. Collection beyond the radius of the item of interest causes minimal errors [22]. That being said, Fig. 16 is a combination of statistical and systemic error from choosing wrong center, not capturing whole profile, asymmetries, etc. If only statistical noise is present, there is only about a 2.5%-5% difference in profile area error [22]. To clarify, this is not the value of each point, but the sum of the relative errors of every point in a profile. This analysis will proceed under the assumption only statistical noise contributed significantly to error due to alignment and calibration procedures. The values present in Fig. 16 are presented to emphasize the importance of proper calibration and alignment of this diagnostic.

However, what this error translates into in terms of eV is dependent on the specific value of the intensity since the relationship between ratio and eV is non-linear. This can be mitigated by the use of multiple line ratios to minimize the effect of the error involved in the use of an Abel inversion. It is effectively increasing the sample size attempting to calculate the electron temperature of each point. However, there is computational cost associated with this, so analysis with a significant number of lines may take a prohibitive amount of either time or computational power. This must be a consideration for implementation of any technique, and may in the case of this diagnostic preclude fast results with a sufficient number of lines, even after code optimization.

In addition to the normal concerns with any experimental data collection due to human imperfection during setup, the analysis relies on the assumption that the involved plasma is optically thin for the wavelengths of interest. While gas pressure in the typical test of an electric

propulsive device should be low enough for this assumption to hold as reasonable, deviation from it would affect the resultant recorded intensity. However, if the pressure is known, Chiu et. al. [15] does present an equation to adjust the cross sections from their paper, though it should be noted this was intended for projecting from data collection to a vacuum state.

Uncertainty of the data was calculated via the residuals by treating it as a mean square error calculation. Specifically, the residuals were treated as the mean square error with the population mean as the estimator, so the following calculation held:

$$Residual = MSE = \left(\frac{\sigma}{\sqrt{n}}\right)^2 \quad (74)$$

That being said, standard deviations of the relative error calculated from treating the residuals as a mean square error calculation found that the technique became unreliable above 20-25 eV due to the slopes involved in the ratios. Additional ratios might be able to reduce standard deviation enough that higher eV can be investigated, though anything above 20 eV using the two line ratios used in this paper should be treated as suspect due to the rapidly ballooning confidence intervals. As can be seen back in Fig. 2 & 3, very small changes in the ratio lead to very large changes in the electron temperature that said ratio corresponds to at higher temperatures. On the following pages, Fig. 17-24 show the upper and lower bounds of the electron temperature based on the calculated uncertainty from the residuals.

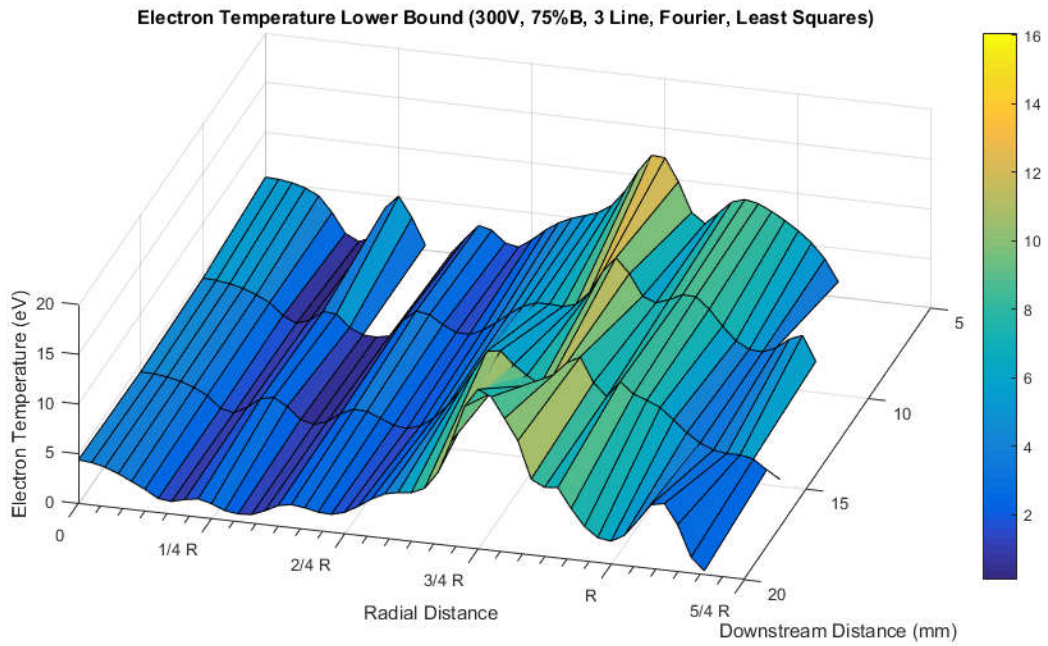


**Fig. 17 300V 75%B Lower Bound, Fourier.**

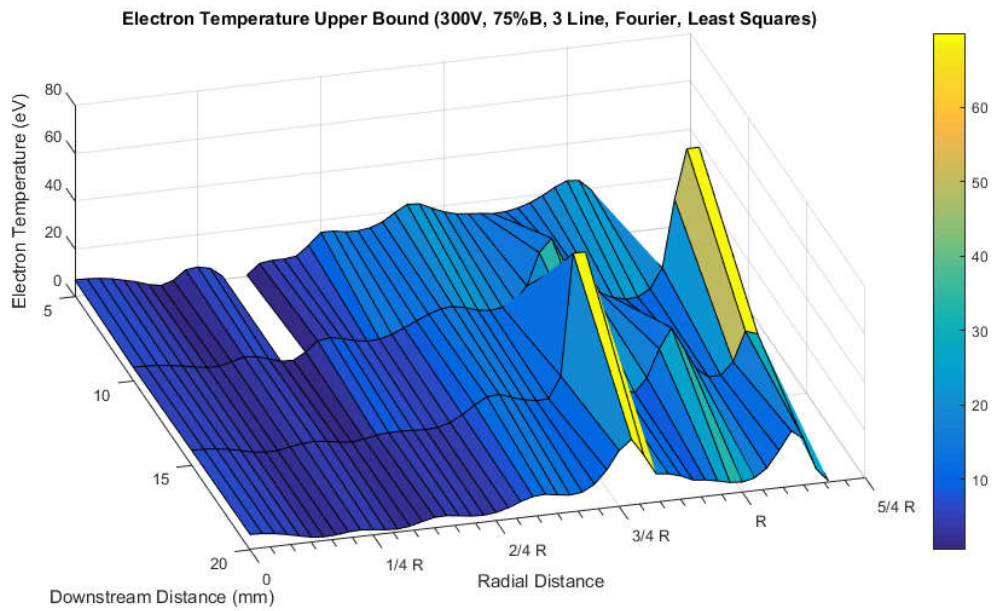


**Fig. 18 300V 75%B Upper Bound, Fourier.**

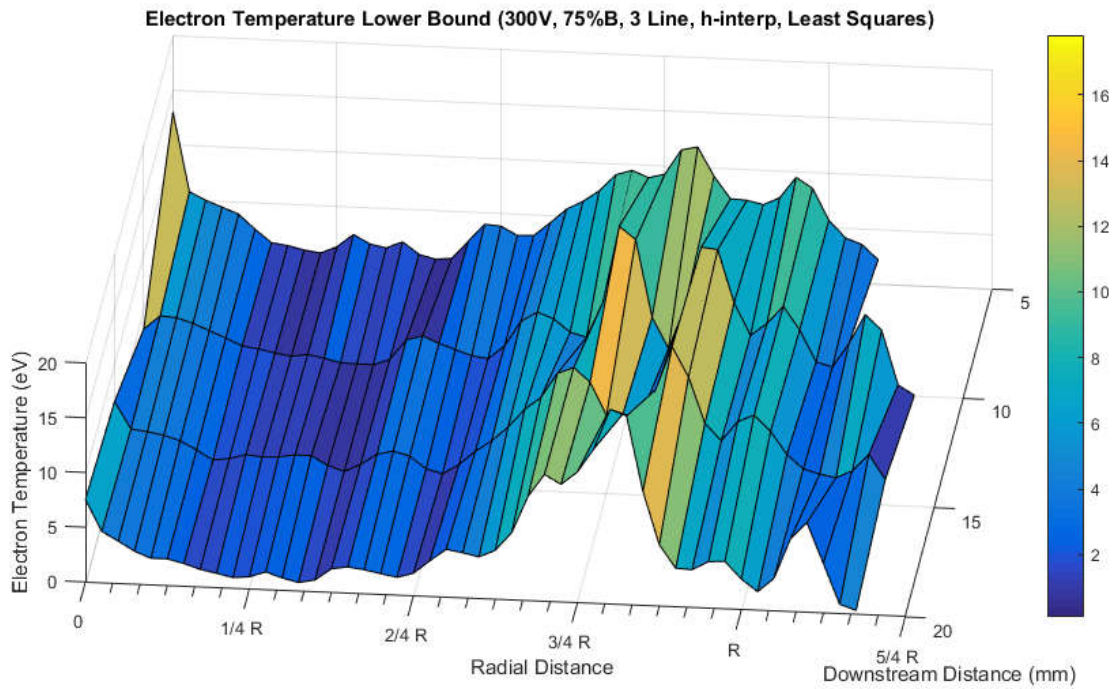


**Fig. 19 300V 75%B Lower Bound, h-interp.**

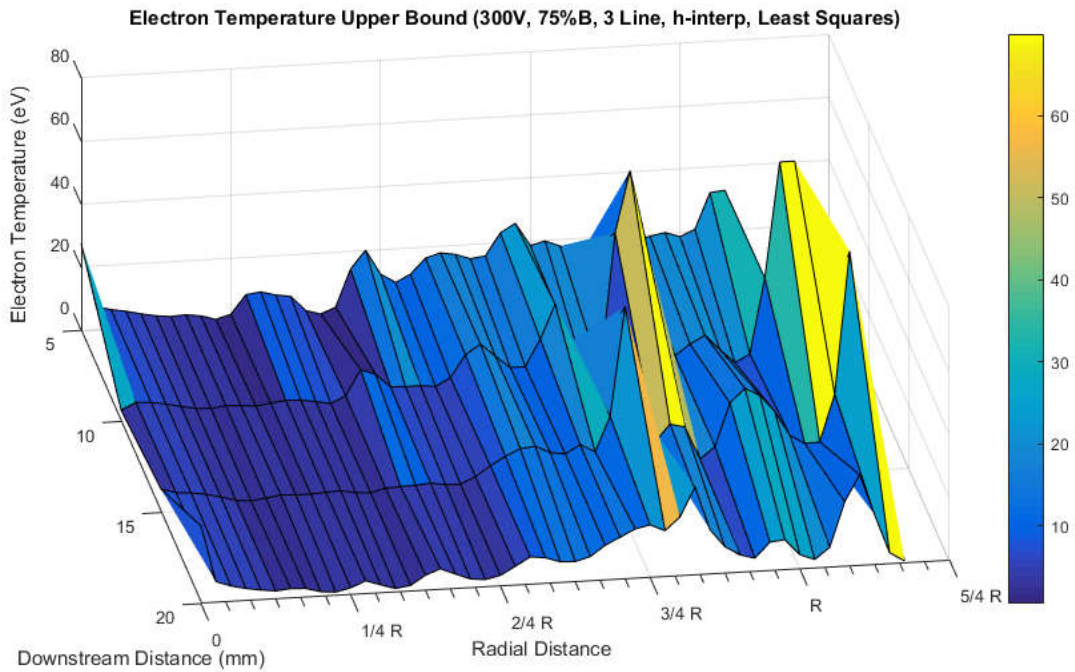


**Fig. 20 300V 75%B Upper Bound, h-interp.**

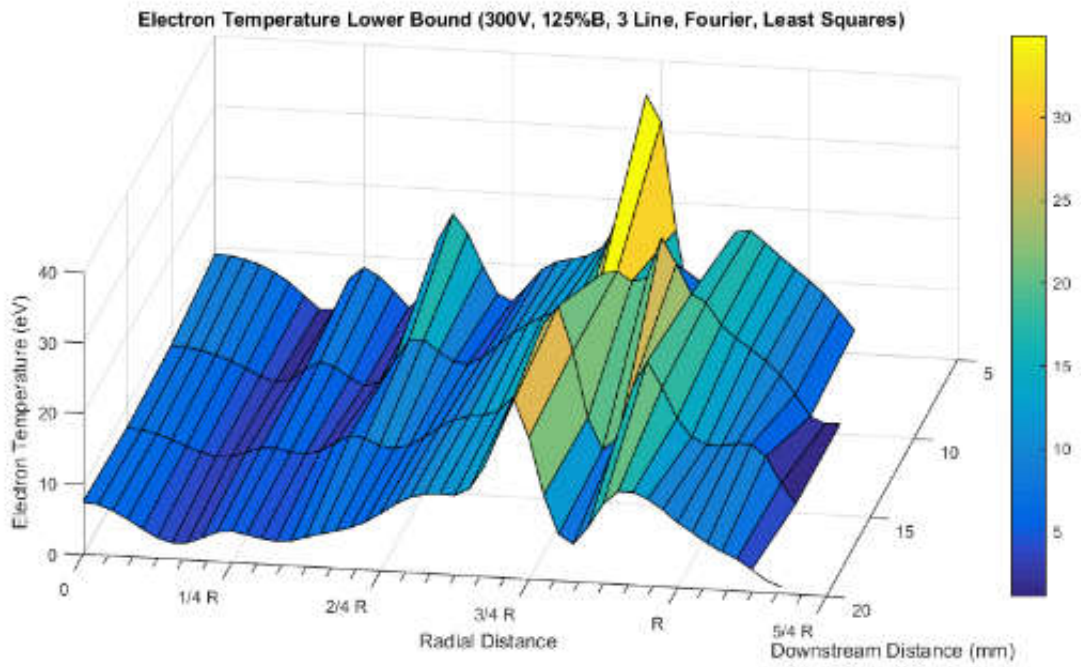


Fig. 21 300V 125%B Lower Bound, Fourier.

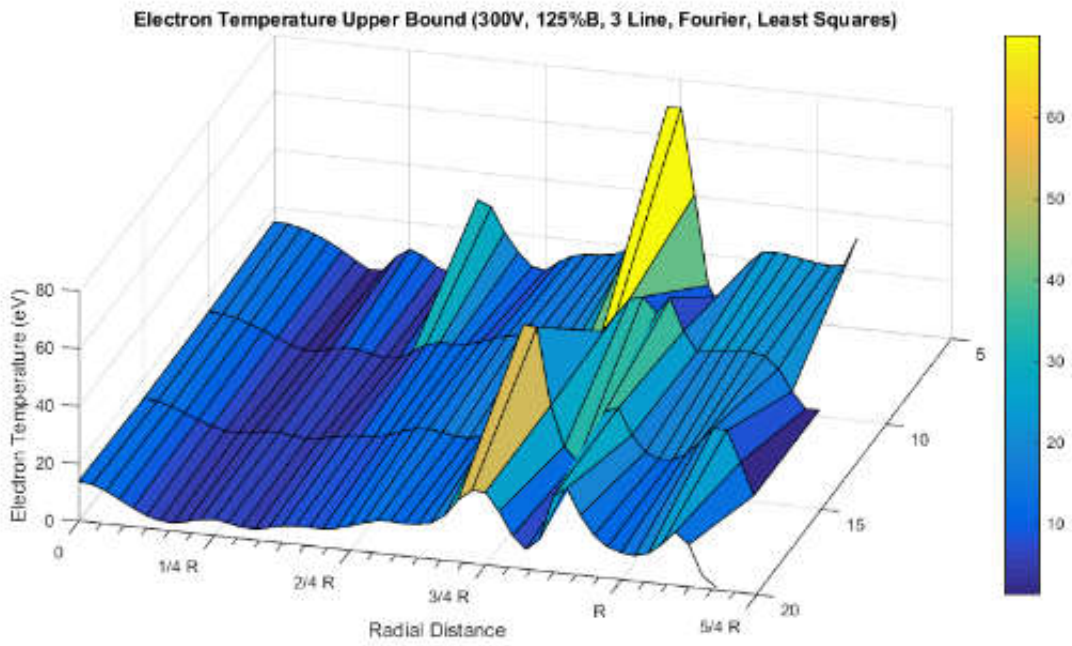


Fig. 22 300V 125%B Upper Bound, Fourier.



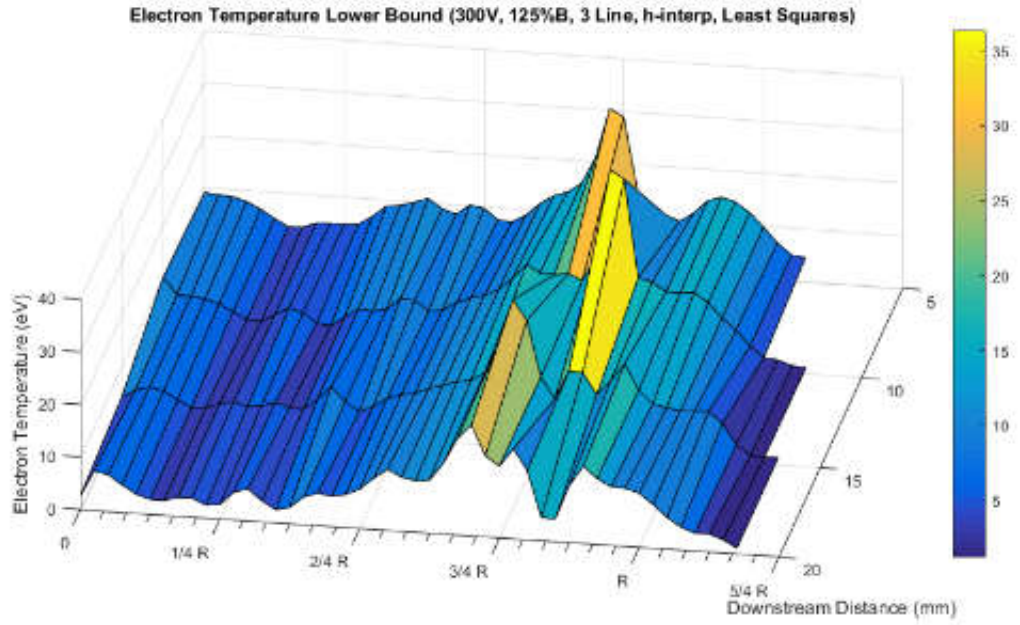


Fig. 23 300V 125%B Lower Bound, h-interp.

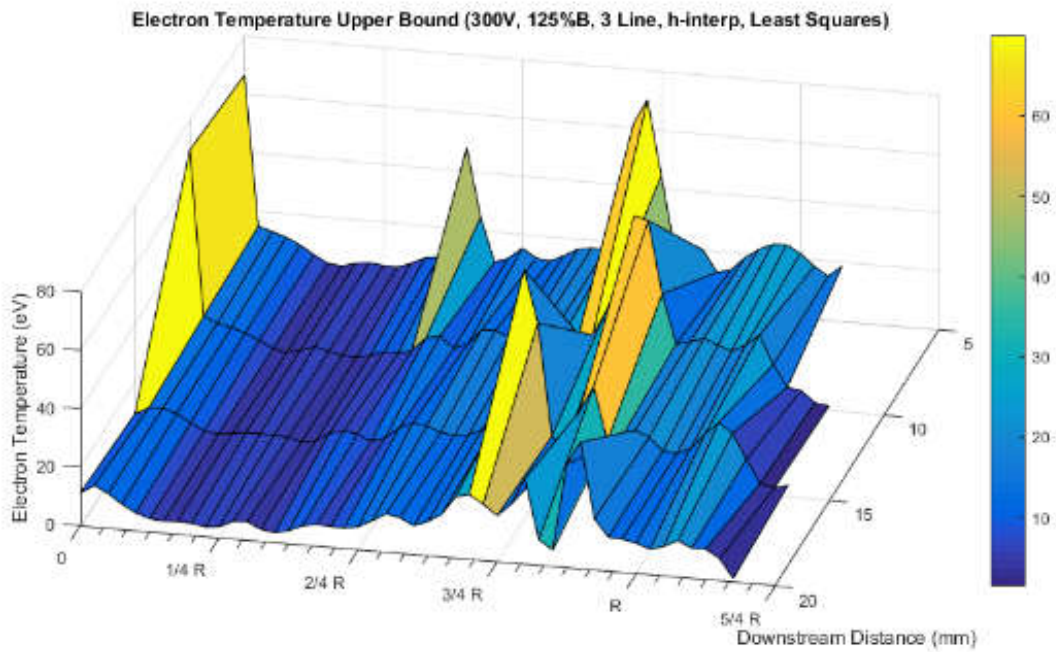


Fig. 24 300V 125%B Upper Bound, h-interp.

The above figures are for the one- $\sigma$  confidence interval. On average, the largest ratio relative errors occurred where the plasma was the thinnest, namely the areas furthest radially from the center of the plume, and areas that had the highest electron temperature. Given the low amount of emission in the areas with thin plasma, enough so that it was beginning to approach being on the order of the noise present in the instrumentation, this is no surprise. Areas of higher electron temperature having higher levels of uncertainty is also expected given the slopes of the equations for the ratio of intensities. However, in areas of lower electron temperature, such as under 10 eV, even fairly large relative error of the intensity ratios does not translate to very large eV error thanks to all the ratios used requiring rather large changes in that region to correspond to an appreciable eV change.

Based on the behavior of the line ratios, the use of a single ratio to determine the electron temperature in a plume is not recommended. Not only will it make readings less accurate, but it will also make it extremely difficult to judge the statistical uncertainty of your measurements. Due to the importance of being able to make an assessment of this, there is a strong incentive for any test facility to pursue use of as many lines as possible with what data collection setups are feasible for the facility and thruster in question. This may be of some difficulty, as many other lines that the collisional radiative model would be currently applicable to are faint enough that care must be taken that the data is not dominated by noise.

Another source of potential systemic error is if the spectrometer used for data collection has effectively different sensitivity to different wavelengths. Care must be taken to account for this, since if a significant difference exists, intensity ratios would be affected. Difference in sensitivity for the selected wavelengths used in this study on the spectrometer employed were insignificant, meaning that no adjustment of data was required to reflect differing sensitivity.

Finally, optical considerations have to be made. A given optical setup is able to resolve only so much. One possible reason for the spikes in the analysis done with h-interpolation is higher frequency data causing problems with the method of Abel inversion. Abel inversion in general is rather sensitive to the slope of the data involved, thus extreme differences require much finer placement of data points. However, this is restricted by the optical capacity of a given setup. Data collection may be modeled as taking a reading at along an infinitesimally thin line, but this is obviously not the case. For especially chaotic thrusters then, much better optical setups and closer packed data points are required.

## **CHAPTER VI**

### **CONCLUDING REMARKS**

Overall, the results seem rather suggestive that the technique is quite useful for near field plasma measurements, which would be rather convenient for testing. While concerns remain, such as the fact custom coding must be used and that above certain eV ranges the technique becomes insensitive, the low cost and non-intrusive nature of the technique means that this technique can be easily added to any existing testing to provide an additional diagnostic. Even if the involved research team felt that it was insufficient for any areas of unexpected behavior, it would be able to provide a means to cheaply determine areas that required more in-depth measurement with devices deemed to be appropriate.

The technique is not appropriate for parts of the plume where plasma is especially thin and the closest planes to the exit plane would require further refinement of technique to be accessible. Careful consideration must be taken to ensure that the optical setup is correct for the nature of the thruster being investigated, and calculations can be time intensive if the strength and the shape of the electric and magnetic fields cannot be provided. However, readings uncorrected for drift may be made until such information is provided, or estimates can be made. Thus even if this would provide values that might be considered untrue, it may still suffice to assist in finding areas of interest to devote more resources towards.

Further investigation could proceed in regards to observing the behavior at additional operating conditions, and implementation of appropriate setups to gather data points for additional lines. Of great interest would be the collection of data at finer spacing and more points further downstream. In addition, it would be recommended to only use the Fourier method of Abel inversion, due to the reduction of errors and ability to filter if needed to adjust for the resolution capacity of the optical collection system being used. The main use of h-interpolation in this study was to check for profile self-consistency between methodologies. If the computation time and resources are available, it likely is worthwhile for an investigator to use two techniques at the same time as a consistency check as well, but it is not a required part of the implementation.

Another possible extension is the possibility of using wavelength filtered photographs to be able to capture large sections of the plume at once. The basic concept would be the same, however careful calibration and calculation would be required to ensure that the proper distances are known and in focus. In addition, care must be taken to ensure no artificial non-uniform dimming occurs due to the camera or filters. The advantages of this approach would be that, as mentioned, would capture large portions of the plume at once. In addition, this would take much less time to gather data than the spectrometer approach, as only several images would be needed. The downsides are that previously mentioned difficulties and the fact that one would not be able to take differently filtered photographs at the same time from the exact same position. This means that there is greater error possibility if either the plume is sufficiently different from the axisymmetric assumption with a two camera arrangement, or time dependent differences from the duration it takes to change one filter to another.

If the issues of a filtered photography-based method can be resolved, this would remove one of the major problems standing in the way of near real time calculation and display of the electron temperature of the plume. Initial attempts were made to attempt this means of gathering intensity data, but unfortunately the equipment on hand and level of practical development of the extension during the times testing of the thruster was underway proved to be insufficient for the task. However, the end result was highly suggestive of the technique being viable should specific technical concerns be resolved.

Finally, it is highly recommended that further investigation into the effects of the ratio of the strengths of the magnetic and electric field be pursued in greater depth, especially in regards to thrusters intended to be throttled. While it may turn out that current simulation data and models might be able to fully capture the differences in behavior in a manner sufficient for engineering, this needs to be verified to confidence levels sufficient for application to design of crewed missions. There may well be parameters that cause excessive wear that should be avoided when human life is potentially on the line. This would be of extreme concern if such a setting existed between two useful operational modes. While careful modulation of the fields could allow one to transition from one mode to the other and completely avoid the configuration of concern, if it was not known about, it is most likely the 'natural' path between two states might be taken. This path might take the thruster through the settings that caused issue.

## REFERENCES

- [1] M. Martinez-Sanchez and J. E. Pollard, "Spacecraft Electric Propulsion-An Overview," *Journal of Propulsion and Power*, vol. 14, no. 5, pp. 688-699, 1998.
- [2] M. Choi, J. Yim, G. Williams, D. Herman and J. Gilland, "Hybrid-PIC Simulation of Backspattered Carbon Transport in the Near-Field Plume of a Hall Thruster," in *35th International Electric Propulsion Conference*, Atlanta, GA, 2017.
- [3] D. Herman, R. Shastry, W. Huang, G. Soulas and H. Kamhawi, "Plasma Potential and Langmuir Probe Measurements in the Near-field Plume of the NASA-300M Hall Thruster," in *48th AIAA/ASME/SAE/ASEE Joint Propulsion Conference & Exhibit*, Atlanta, GA, 2012.
- [4] H. Kamhawi, W. Huang, J. Gilland, T. Haag, J. Mackey, J. Yim, L. Pinero, G. Williams, P. Peterson and D. Herman, "Performance, Stability, and Plume Characterization of the HERMeS Thruster with Boron Nitride Silica Composite Discharge Channel," in *35th International Electric Propulsion Conference*, Atlanta, GA, 2017.
- [5] A. L. Ortega, I. G. Mikellides and V. H. Chaplin, "Numerical Simulations for the Assessment of Erosion in the 12.5-kW Hall Effect Rocket with Magnetic Shielding (HERMeS)," in *35th International Electric Propulsion Conference*, Atlanta, GA, 2017.
- [6] J. P. Boeuf, "Tutorial: Physics and modeling of Hall thrusters," *Journal of Applied Physics*, vol. 121, no. 1, p. 011101, 2017.
- [8] R. Harris, *Modern Physics*, 2nd ed., San Francisco: Pearson Education, 2008.

- [9] NASA, Washington, D.C.: NASA, 2017.
- [10] B. Gerstenmaier, *Progress in Defining the Deep Space Gateway and Transport Plan*, Washington, D.C.: NASA, 2017.
- [11] G. Sutton and O. Biblarz, *Rocket Propulsion Elements*, Hoboken: John Wiley and Sons, 2010.
- [12] R. Jahn, *Physics of Electrical Propulsion*, Mineola: Dover Publications, 2006.
- [13] W. Demtröder, *Laser Spectroscopy*, 3rd edition, Berlin: Springer-Verlag, 2002.
- [14] G. F. Karabadzhak, Y. Chiu and R. A. Dressler, "Passive Optical Diagnostic of Xe Propelled Hall Thrusters. II. Collisional Radiative Model," *Journal of Applied Physics*, vol. 99, no. 11, p. 113305, 2006.
- [15] Y. Chiu, B. L. Austin, S. Williams, R. A. Dressler and G. F. Karabadzhak, "Passive Optical Diagnostic of Xe-Propelled Hall Thrusters. I. Emission Cross Sections," *Journal of Applied Physics*, vol. 99, no. 11, p. 113304, 2006.
- [16] R. Shastry, *Experimental Characterization of the Near-Wall Region in Hall Thrusters and Its Implications on Performance and Lifetime*, Ann Arbor, Michigan: University of Michigan Dept. of Aerospace Engineering, 2011.
- [17] G. Pretzier, "A New Method for Numerical Abel-Inversion," *Zeitschrift für Naturforschung A*, vol. 46, no. 7, p. 639–641, 1991.
- [18] T. W. Haag, "Thrust Stand for High-Power Electric Propulsion Devices," *Review of Scientific Instruments*, vol. 62, no. 5, p. 1186, 1991.



- [19] G. Williams, H. Gilland, P. Peterson, H. Kamhawi, W. Huang, D. Ahren, J. Yim, D. Herman, R. Hofer and M. Sekerak, "Wear Testing of the HERMeS Thruster," in *52nd AIAA/SAE/ASEE Joint Propulsion Conference*, Salt Lake City, 2016.
- [20] R. Shastry, W. Huang, D. Herman, G. Soulas and H. Kamhawi, "Plasma Potential and Langmuir Probe Measurements in the Near-field Plume of the NASA-457Mv2 Hall Thruster," in *48th AIAA/ASME/SAE/ASEE Joint Propulsion Conference & Exhibit*, Atlanta, GA, 2012.
- [21] R. Shastry, W. Huang, T. W. Haag and H. Kamhawi, "Langmuir Probe Measurements Within the Discharge Channel of the 20-kW NASA-300M and NASA-300MS Hall Thrusters," NASA, Brook Park, 2013.
- [22] G. Pretzier, H. Jäger, T. Neger, H. Philipp and J. Woisetschläger, "Comparison of Different Methods of Abel Inversion Using Computer Simulated and Experimental Side-On Data," *Zeitschrift für Naturforschung A*, vol. 47, no. 9, 1992.
- [23] M. Matsui, S. Yakoto, H. Takayanagi, H. Koizumi, K. Komurasaki and Y. Arakawa, "Plume Characterization of Plasma Thrusters Using Diode-Laser Absorption Spectroscopy," in *44th AIAA Aerospace Sciences Meeting and Exhibit*, Reno, NV, 2006.
- [24] A. Kramida, Y. Ralchenko, J. Reader and NIST ASD Team (2015), *NIST Atomic Spectra Database (ver. 5.3)*, Gaithersburg, MD: National Institute of Standards and Technology, 2015.
- [25] NASA, *NASA Glenn's Hall Thruster*, Brook Park, Ohio: NASA, 2017.

- [26] P. Peterson, H. Kamhawi, W. Huang, J. Yim, D. Herman, G. Williams and J. Gilland,  
"NASA HERMeS Hall Thruster Electrical Configuration," in *52nd AIAA/SAE/ASEE  
Joint Propulsion Conference*, Salt Lake City, 2016.

## **APPENDICIES**

## **APPENDIX A**

### **Additional Data**

The following is data collected on different operational parameters of the TDU-3 at roughly 5mm downstream from the exit plane. The following was not presented in the main body, as full profiles at multiple downstream distances do not exist for several reasons. The data was collected during initial conceptualization and troubleshooting of the code and procedures. Also, it is not directly comparable in terms of reliability to the data presented in the main body, as it was determined that data collection did not extend to the edge of the plume at the downstream distance the observations were made. As discussed in the section on error considerations, this can greatly affect the resultant Abel inversion. In addition, the proper treatment of sensor gains for weaker emission lines was not definitively established until after the data below was collected, thus only one ratio was able to be used for analysis. Due to this fact, it does not have a proper means to calculate a confidence interval in the same manner as the main analysis.

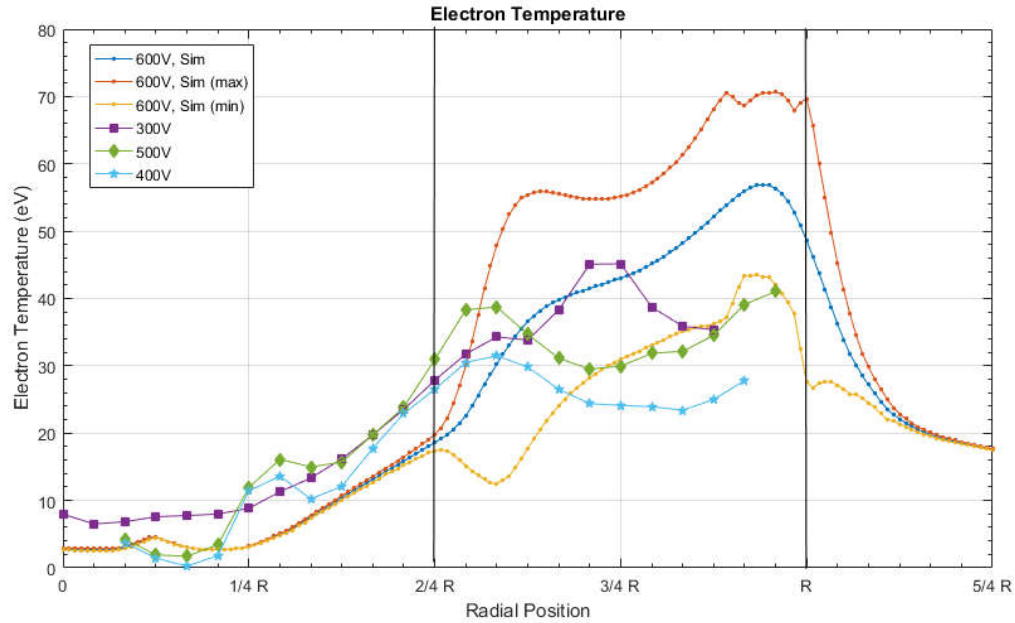


**Fig. 25 Comparative Electron Temperature**

As can be seen in Fig. 25 and was already mentioned, data collection did not extend far enough radially due to track limits on the linear movement stage. Unfortunately, this was only discovered after the vacuum chamber was sealed, and as such no adjustments to the stage could be made until the scheduled test runs were concluded. Originally it was thought that extending data collection to the edge of the channel would be sufficient, but this proved to not be the case. It is recommended for any other individual utilizing such a technique that  $5/4 R$  be treated as the absolute minimum distance to extend data collection in the domain of 1-30mm from the exit plane of the thruster. Further distances downstream would require data to be collected at further radial distances from the centerline.

Simulation data was provided courtesy of Dr. Maria Choi for the 600V case. Unfortunately, simulation data for exact matches in operational parameters did not exist, so comparisons using the closest simulation data had to be used in the paper proper. The simulation data was deemed sufficiently different in parameters from the final data presented in the main body to prevent meaningful comparison with the simulation data.

## APPENDIX B

### Complimentary Diagnostic Proposal

In this section a complimentary absorption spectroscopy diagnostic to the main emission diagnostic outlined in the main section is proposed. Due to limitations in time and equipment availability, it was not pursued in the main body of the study. At the current time, this methodology is untested, but a tabletop proof of concept verification could be performed with a xenon optogalvanic lamp. That being said, the information and proposal presented here is of a simplified nature, thus further consideration would need to be taken to implement the following diagnostic.

The number density of the various species of xenon is of utility for the types of application mentioned in this study, though unfortunately this is again hard to record without disturbing the plasma in some manner or otherwise being intrusive to an experiment. However, it seems feasible to gather this information using non-intrusive methods, such as with absorption spectroscopy. If we wish to calculate the number density, we must derive the relationship between laser intensity, its absorption, and said number density. Given that the relationship between probe laser intensity  $I$  and absorption coefficient  $k(x)$  is expressed by the Beer-Lambert law [13]:

$$\frac{dI}{dx} = -k(x)I \quad (75)$$

Absorption properties in a Hall thruster plume area assumed to be axisymmetric, local absorption coefficient  $k_r(r)$ , where  $r$  is the radial coordinate, can be obtained via an Abel inversion [23]:

$$k_f(r) = \frac{1}{\pi} \int_r^R \frac{d\left(\ln\left(\frac{I}{I_0}(y)\right)\right)}{dy} \frac{dy}{\sqrt{y^2 - r^2}} \quad (76)$$

If a Boltzmann relation is assumed between absorbing and excited states, integrated absorption coefficient  $K(r)$  is expressed as a function of the number density of the absorbing state  $n_a(r)$  [23]:

$$K(r) = \int_{-\infty}^{+\infty} k_f(r) df = \frac{\lambda^2}{8\pi} \frac{g_e}{g_a} A_{ea} n_a(r) \left[ 1 - e^{\frac{-\Delta E_{ae}}{k_{B,1} T_{e,1}}} \right] \quad (77)$$

Where  $g$  should be corrected from  $g=2J+1$  to  $g=(2J+1)(2I_m+1)$  when nuclear spin has a non-zero value [23] and  $\lambda$  is the wavelength associated with the absorption line related to the state transition. However Eq. 77 is still valid because both absorbing and excited states have common  $I_m$ . [23] Solving for  $n_a$  we get:

$$\frac{K(r)}{\frac{\lambda^2}{8\pi} \frac{g_e}{g_a} A_{ea} \left[ 1 - e^{\frac{-\Delta E_{ae}}{k_{B,1} T_{e,1}}} \right]} = n_a(r) \quad (78)$$

Thanks to the Boltzmann relation assumption, total number density  $n_{tot}$  can be calculated from the measured number density [23]:

$$n_{tot} = \frac{n_a}{g_a} \sum_i g_i e^{\frac{-\Delta E_{ia}}{k_{B,1} T_{e,1}}} \quad (79)$$

Where the summation  $i$  is taken for all states [23]. Substituting in Eq. 76 and Eq. 77:

$$n_{tot}(r) = \frac{8 \int_{-\infty}^{+\infty} \int_r^R \frac{d\left(\ln\left(\frac{I}{I_0}(y)\right)\right)}{dy} \frac{1}{\sqrt{y^2 - r^2}} dy df}{\lambda^2 g_e A_{ea} \left[ 1 - e^{\frac{-\Delta E_{ae}}{k_{B,1} T_{e,1}}} \right]} \sum_i g_i e^{\frac{-\Delta E_{ia}}{k_{B,1} T_{e,1}}} \quad (80)$$

The exact lines to be examined, and their Einstein coefficients are taken from the NIST spectra database [24]. Care must be taken to ensure that these lines correspond only to a single

level of ionization, and are sufficiently different in wavelength from any neighboring lines that a spectrometer can resolve the changes in the line of interest.

The experiment would take place in a tabletop setup environment in this proposal, as this would be intended as a proof of concept test. That being said, the test itself would consist of using a tunable laser diode to sweep across frequencies of interest with the beam passing through a test object; in the case of the tabletop experiment an optogalvanic tube containing xenon and barium. The laser source and some of the initial measurement pickups should be contained in an optical cage for safety.

Starting from the laser source, to be able to properly determine if the laser is at the correct frequency and compare the intensity before and after passing through the test object, the laser must be split. Specifically, it must be split off to have its wavelength and intensity measured prior to probing the object of interest. Once this is done, the resulting beam leg that has not been directed towards a power meter or wavelength meter must exit the optical cage through a shutter, at which point it is collimated. Once this is complete, the beam is split, with one leg going to a photodiode, and the other passing through the optogalvanic tube. The laser that has passed through the tube would then be directed at another photodiode. Of note is that before all pickups and photodiodes should be a neutral density filter. Also of note is that before each photodiode, the beam would be split, with one leg going to the diode, the remainder going to a beam-dump.

A lock-in amplifier would be used to ensure that the beams were being properly lined up in terms of phase, and then would be fed into a spectrometer. The tunable diode laser would be controlled through a thermal controller and current controller which would be modulated using



a function generator. The meters, photogalvanic tube, the spectrometer, and the controllers will be hooked up to a computer for control and data collection.

The frequency of the laser will be swept back and forth across the wavelengths of interest in a manner controlled by the function generator. The exact manner in which it is swept will be monitored by the previously mentioned wavelength meter. This will allow proper correlation of the gathered intensity data with wavelength instead of simply time. The specific wavelengths of interest are noted in Table 1. These are not determined by any exclusive need, so if other wavelengths are of more benefit to the investigator, there is no reason not to pursue them.

<b>Wavelength</b>	<b>Associated Item</b>
680.762 nm	Xe II
728.230 nm	Ba I
841.150 nm	Xe I

**Table 1. Absorption Wavelengths.**

## APPENDIX C

### MATLAB Code

```
function [eV_fourier_matrix,x2val_fourier,
eV_interp_matrix,x2val_interp]=getIntensity(h_matrix_raw,E,B,a,step,
downstream_step,number_terms)
%Uses the following assumptions:
%Both data sets same size and same evenly spaced
%Data arranged in variable from top to bottom with top being center
%Peter Joseph Urban-2018

%suppress the warnings get from the integration due to end conditions
warning('off','all')

%The input variables
h_matrix_raw; %Your raw data.
E; %Electric field strength, matrix
B; %Magnetic field strength, matrix
a; %Ion ratio, matrix
step; %Distance between points across plume
downstream_step; %Downstream distance between planes
number_terms; %Number of cosine terms using fourier.

power=1; %Don't touch unless have to.

%[row,column,page]
%This assumes left is thruster, top is centerline
sz = size(h_matrix_raw);
lines=sz(3);
downstream_points = sz(2);
width = sz(1);

h_matrix=h_matrix_raw;

%Normalize the ends
for n=1:lines
    for m=1:downstream_points
        h_matrix(:,m,n)=h_matrix(:,m,n)-h_matrix(width,m,n);
    end
end

%Intensity function. This is the raw deal, not precalculated
fun=@(Te,wavelengthOfInterest,E,B,a)getIntensity(Te,wavelengthOfInterest,E
,B,a);

%Initialize your intensity matrices
I_interp=zeros(sz);
I_fourier=zeros(sz);

%Get your point intensity matrixes. Note, this is a multi-dimensional
%matrix, where the pages are the wavelength
for n=1:lines
    if h_matrix(1,1,n)==0
        %do nothing if closest center most h-value is 0. This should only
```

```

        %happen if there IS nothing at that wavelength
    else
        for m=1:downstream_points

I_interp(:,m,n)=experimental_abel_inversion_spectra(h_matrix(:,m,n),power,
step)';
            I_fourier(:,m,n)=abel_inversion(h_matrix(:,m,n).^power,(width-
1)*step,number_terms,0,0).^ (1/power);
        end
    end
end
%Initialize your storage matrices
eV_fourier_matrix=zeros([width downstream_points]);
x2val_fourier=zeros([width downstream_points]);
eV_interp_matrix=zeros([width downstream_points]);
x2val_interp=zeros([width downstream_points]);

%Relative Average Least Squares to find eV. x2val is the residual,
%currently needs new lines manually added in
%Fourier
for m=1:downstream_points
    for l=1:width

[eV_fourier_matrix(l,m),x2val_fourier(l,m)]=fminbnd(@(x)1./2.*(((I_fourier
(l,m,2)./I_fourier(l,m,3)-
fun(x,2,E(l,m),B(l,m),a(l,m))/fun(x,3,E(l,m),B(l,m),a(l,m))).^2)./(I_four
ier(l,m,2)./I_fourier(l,m,3)).^2)+((I_fourier(l,m,5)./I_fourier(l,m,3)-
fun(x,5,E(l,m),B(l,m),a(l,m))/fun(x,3,E(l,m),B(l,m),a(l,m))).^2)./(I_four
ier(l,m,5)./I_fourier(l,m,3)).^2)),.1,70);
        end
    end
%h-interp
for m=1:downstream_points
    for l=1:width

[eV_interp_matrix(l,m),x2val_interp(l,m)]=fminbnd(@(x)1./2.*(((I_interp(l,
m,2)./I_interp(l,m,3)-
fun(x,2,E(l,m),B(l,m),a(l,m))/fun(x,3,E(l,m),B(l,m),a(l,m))).^2)./(I_inte
rp(l,m,2)./I_interp(l,m,3)).^2)+((I_interp(l,m,5)./I_interp(l,m,3)-
fun(x,5,E(l,m),B(l,m),a(l,m))/fun(x,3,E(l,m),B(l,m),a(l,m))).^2)./(I_inte
rp(l,m,5)./I_interp(l,m,3)).^2)),.1,70);
        end
    end
end
%
%You're ready to display your data. Warning, you've probably got sections
%of bad numbers in the low density regions. Easy to tell due to horribly
%large residuals.

%restore warnings
warning('on','all')
end

```

```

function [intensity]=getIntensity(Te,wavelengthOfInterest,E,B,a)
%Calculates the intensity of an emissssion line given a unit volume of
%unit density of xenon and electrons.
%Peter Joseph Urban-2018

Te; Electron temperature
wavelengthOfInterest; %See list below
E; %Electric field strength, matrix
B; %Magnetic field strength, matrix
a; %Ion ratio, matrix

%Wavelength of Interest
%1=788.7nm
%2=823.2nm
%3=828.0nm
%4=834.7nm
%5=881.9nm
%6=904.5nm
%7=916.3nm
%8=980.0nm

%Declare Constants
k=8.61733035*10^-5; %Boltzmann constant in eV per K
me=9.1093835611*10^-31; %Rest Mass of Electron in kg
mXe=2.180173045*10^-25; %Mass of Xe in kg
eVtoK=1.160450520*10^4; %eV to Kelvin conversion factor
h=6.62607004081*10^-34; %Planck's constant
c=299792458; %Speed of light, m/s
eVtoKG=1.782662*10^-36; %eV to kg conversion factor
KGtoEv=1/eVtoKG;
MomentToEv=1/(5.344286*10^-28);
JToEv=6.241509*10^18;

cmsToms=0.0001; %cm^2 to m^2
chartScale=10^-18;

%Drift Velocity
ElecVel=(E*B)/(B.^2);
DelE=0.5*me*ElecVel.^2*JToEv;

%Wavelength list, includes all listed in cross section pap
wavelength=[788.7*10^-9 823.2*10^-9 828*10^-9 834.7*10^-9 881.9*10^-9
904.5*10^-9 916.3*10^-9 980*10^-9 462.4*10^-9 467.1*10^-9 473.4*10^-9
480.7*10^-9 484.4*10^-9 492.1*10^-9 497.3*10^-9 504.5*10^-9 519.1*10^-9
526.2*10^-9 529.2*10^-9 541.9*10^-9];

%eV Table values from paper
eV=[10 12 15 17 19 21 23 25 27 29 31 35 40 45 50 55 60 65 70 80 90 100 110
120 130 140 150 160 170 180 190 200];

%Load cross section data, not included
load('crossSecTable.mat');

%Various Ke0 functions

```

```

fun1 = @(Ee,Te)
sqrt((2.*Ee)./(me.*KGtoEv)).*sqrt(1./(pi*((Te*Dele)))).*exp(-
(Ee+Dele)./(Te)).*(sinh(2*sqrt(Ee.*Dele)./Te)).*(crossSec788_7(Ee).*chartS
cale.*cmsToms);
fun2 = @(Ee,Te)
sqrt((2.*Ee)./(me.*KGtoEv)).*sqrt(1./(pi*((Te*Dele)))).*exp(-
(Ee+Dele)./(Te)).*(sinh(2*sqrt(Ee.*Dele)./Te)).*(crossSec823_2(Ee).*chartS
cale.*cmsToms);
fun3 = @(Ee,Te)
sqrt((2.*Ee)./(me.*KGtoEv)).*sqrt(1./(pi*((Te*Dele)))).*exp(-
(Ee+Dele)./(Te)).*(sinh(2*sqrt(Ee.*Dele)./Te)).*(crossSec828(Ee).*chartSca
le.*cmsToms);
fun4 = @(Ee,Te)
sqrt((2.*Ee)./(me.*KGtoEv)).*sqrt(1./(pi*((Te*Dele)))).*exp(-
(Ee+Dele)./(Te)).*(sinh(2*sqrt(Ee.*Dele)./Te)).*(crossSec834_7(Ee).*chartS
cale.*cmsToms);
fun5 = @(Ee,Te)
sqrt((2.*Ee)./(me.*KGtoEv)).*sqrt(1./(pi*((Te*Dele)))).*exp(-
(Ee+Dele)./(Te)).*(sinh(2*sqrt(Ee.*Dele)./Te)).*(crossSec881_9(Ee).*chartS
cale.*cmsToms);
fun6 = @(Ee,Te)
sqrt((2.*Ee)./(me.*KGtoEv)).*sqrt(1./(pi*((Te*Dele)))).*exp(-
(Ee+Dele)./(Te)).*(sinh(2*sqrt(Ee.*Dele)./Te)).*(crossSec904_5(Ee).*chartS
cale.*cmsToms);
fun7 = @(Ee,Te)
sqrt((2.*Ee)./(me.*KGtoEv)).*sqrt(1./(pi*((Te*Dele)))).*exp(-
(Ee+Dele)./(Te)).*(sinh(2*sqrt(Ee.*Dele)./Te)).*(crossSec916_3(Ee).*chartS
cale.*cmsToms);
fun8 = @(Ee,Te)
sqrt((2.*Ee)./(me.*KGtoEv)).*sqrt(1./(pi*((Te*Dele)))).*exp(-
(Ee+Dele)./(Te)).*(sinh(2*sqrt(Ee.*Dele)./Te)).*(crossSec980(Ee).*chartSca
le.*cmsToms);
fun9 = @(Ee,Te)
sqrt((2.*Ee)./(me.*KGtoEv)).*sqrt(1./(pi*((Te*Dele)))).*exp(-
(Ee+Dele)./(Te)).*(sinh(2*sqrt(Ee.*Dele)./Te)).*(crossSec462_4(Ee).*chartS
cale.*cmsToms);
fun10 = @(Ee,Te)
sqrt((2.*Ee)./(me.*KGtoEv)).*sqrt(1./(pi*((Te*Dele)))).*exp(-
(Ee+Dele)./(Te)).*(sinh(2*sqrt(Ee.*Dele)./Te)).*(crossSec467_1(Ee).*chartS
cale.*cmsToms);
fun11 = @(Ee,Te)
sqrt((2.*Ee)./(me.*KGtoEv)).*sqrt(1./(pi*((Te*Dele)))).*exp(-
(Ee+Dele)./(Te)).*(sinh(2*sqrt(Ee.*Dele)./Te)).*(crossSec473_4(Ee).*chartS
cale.*cmsToms);
%placeholder functions
fun12 = 0;
fun13 = 0;
fun14 = 0;
fun15 = 0;
fun16 = 0;
fun17 = 0;
fun18 = 0;
fun19 = 0;
fun20 = 0;

%Calculate ke0 for wavelengths, don't need them for the visible spectrum
%right now

```

```

ke0788_7=integral(@(Ee) fun1(Ee,Te),10,150,'ArrayValued',true);
ke0823_2=integral(@(Ee) fun2(Ee,Te),10,150,'ArrayValued',true);
ke0828=integral(@(Ee) fun3(Ee,Te),10,150,'ArrayValued',true);
ke0834_7=integral(@(Ee) fun4(Ee,Te),10,150,'ArrayValued',true);
ke0881_9=integral(@(Ee) fun5(Ee,Te),10,150,'ArrayValued',true);
ke0904_5=integral(@(Ee) fun6(Ee,Te),10,150,'ArrayValued',true);
ke0916_3=integral(@(Ee) fun7(Ee,Te),10,150,'ArrayValued',true);
ke0980=integral(@(Ee) fun8(Ee,Te),10,150,'ArrayValued',true);
ke0462_4=integral(@(Ee) fun9(Ee,Te),10,150,'ArrayValued',true);
ke0467_1= integral(@(Ee) fun10(Ee,Te),10,150,'ArrayValued',true);
ke0473_4=integral(@(Ee) fun11(Ee,Te),10,150,'ArrayValued',true);
%placeholder ke0s
ke0480_7=0;
ke0484_4=0;
ke0492_1=0;
ke0497_3=0;
ke0504_5=0;
ke0519_1=0;
ke0526_2=0;
ke0529_2=0;
ke0541_9=0;

%ke0, ke1, ke2 storage
ke0=[ke0788_7 ke0823_2 ke0828 ke0834_7 ke0881_9 ke0904_5 ke0916_3 ke0980
ke0462_4 ke0467_1 ke0473_4 ke0480_7 ke0484_4 ke0492_1 ke0497_3 ke0504_5
ke0519_1 ke0526_2 ke0529_2 ke0541_9];
k1=[0.942*sqrt(2*eVtoKG/mXe) 29.23*sqrt(2*eVtoKG/mXe)
3.90*sqrt(2*eVtoKG/mXe) 3.13*sqrt(2*eVtoKG/mXe) 69.11*sqrt(2*eVtoKG/mXe)
18.67*sqrt(2*eVtoKG/mXe) 20.73*sqrt(2*eVtoKG/mXe) 32.71*sqrt(2*eVtoKG/mXe)
0.63*sqrt(2*eVtoKG/mXe) 1.31*sqrt(2*eVtoKG/mXe) 0.19*sqrt(2*eVtoKG/mXe)
0.28*sqrt(2*eVtoKG/mXe) 0.83*sqrt(2*eVtoKG/mXe) 0.58*sqrt(2*eVtoKG/mXe)
0.1*sqrt(2*eVtoKG/mXe) 0.03*sqrt(2*eVtoKG/mXe) 0.29*sqrt(2*eVtoKG/mXe)
0.22*sqrt(2*eVtoKG/mXe) 1.34*sqrt(2*eVtoKG/mXe) 1.02*sqrt(2*eVtoKG/mXe)];
k1=k1.*chartScale.*cmsToms;
k2=[0.244*sqrt(4*eVtoKG/mXe) 10.1*sqrt(4*eVtoKG/mXe) 1*sqrt(4*eVtoKG/mXe)
1.02*sqrt(4*eVtoKG/mXe) 18.31*sqrt(4*eVtoKG/mXe) 5.7*sqrt(4*eVtoKG/mXe)
9.31*sqrt(4*eVtoKG/mXe) 6.75*sqrt(4*eVtoKG/mXe) 1.48*sqrt(4*eVtoKG/mXe)
2.45*sqrt(4*eVtoKG/mXe) 0.23*sqrt(4*eVtoKG/mXe) 0.03*sqrt(4*eVtoKG/mXe)
21.8*sqrt(4*eVtoKG/mXe) 9.4*sqrt(4*eVtoKG/mXe) 3.17*sqrt(4*eVtoKG/mXe)
1.82*sqrt(4*eVtoKG/mXe) 8.83*sqrt(4*eVtoKG/mXe) 8.28*sqrt(4*eVtoKG/mXe)
40.3*sqrt(4*eVtoKG/mXe) 33.6*sqrt(4*eVtoKG/mXe)];
k2=k2.*chartScale.*cmsToms;

%Set to 1 if its not a line affected by the metastable lines
gamma=[1 1.89 1 1 1.016 3.754 2.632 2.430 1 1 1 1 1 1 1 1 1 1 1];

%Intensity calcs
intensityPre1=ke0(wavelengthOfInterest)+a*k1(wavelengthOfInterest)+(1-
a)/2*k2(wavelengthOfInterest);
intensityPre2=intensityPre1*h*c/(4*pi*wavelength(wavelengthOfInterest));

%Metastable calcs
sum=(ke0(2)+a*k1(2)+(1-a)/2*k2(2))+(ke0(5)+a*k1(5)+(1-
a)/2*k2(5))+(ke0(6)+a*k1(6)+(1-a)/2*k2(6))+(ke0(7)+a*k1(7)+(1-
a)/2*k2(7))*(1/9.9*(1/916.3)*840.9)+(ke0(8)+a*k1(8)+(1-a)/2*k2(8));

```

```
%More metastable calcs

Kwave=sum/(ke0(wavelengthOfInterest)+a*k1(wavelengthOfInterest)+(1-
a)/2*k2(wavelengthOfInterest));

%Meta stable adjust
if
wavelengthOfInterest==1||wavelengthOfInterest==3||wavelengthOfInterest==4
    Kwave=0;
end

%Return intensity
intensity=intensityPre2*(1+Kwave/gamma(wavelengthOfInterest));
end
```

```

function [Intense]=experimental_abel_inversion_spectra(h1,power,step)
%h-interpolation based abel inversion
%Note: this thing is SLOOOOOOW when gets into any noise dominated areas

h1; %End normalized data
power; %Don't touch unless have to.
step; %Distance between points across plume

I=h1.^power;

%Get sizes and such, has some leftover from attempts at camera
sz = size(I);
height = sz(2);
width = sz(1);
center=width;

right=width;

%Set up coordinate system
testX=linspace(0,center-1,center)';
%This step not as needed for keeping track of stuff if not camera
testY=I;

%Set-up smoothing spline
testFunction=fit(testX,testY,'smoothingspline');
%Calc derivative
deriv=differentiate(testFunction,testX)./step;
testDerivative=fit(testX,deriv,'smoothingspline');

%Define abel inversion
abelFunc= @(x,r) testDerivative(x)/sqrt(x^2-r^2);

%Do inversion
for n=0:right-1
qright(n+1)=-1/pi.*integral(@(x) abelFunc(x,n),n,right-
1,'ArrayValued',true);
end

%Approximate for the center of the radius
qright(1)=-1/pi.*integral(@(x) abelFunc(x,0),0.00000000001,right-
1,'ArrayValued',true);
qright(right)=-1/pi.*integral(@(x) abelFunc(x,right-1),right-1-
0.00000000001,right-1,'ArrayValued',true);

%Return value
qright=qright.^(1/power);
Intense=qright;
end

```



This copyright notice applies to all code following this point in this appendix.

Copyright (c) 2016, Carsten Killer  
All rights reserved.

Redistribution and use in source and binary forms, with or without modification, are permitted provided that the following conditions are met:

- \* Redistributions of source code must retain the above copyright notice, this list of conditions and the following disclaimer.
- \* Redistributions in binary form must reproduce the above copyright notice, this list of conditions and the following disclaimer in the documentation and/or other materials provided with the distribution
- \* Neither the name of the University of Greifswald nor the names of its contributors may be used to endorse or promote products derived from this software without specific prior written permission.

THIS SOFTWARE IS PROVIDED BY THE COPYRIGHT HOLDERS AND CONTRIBUTORS "AS IS" AND ANY EXPRESS OR IMPLIED WARRANTIES, INCLUDING, BUT NOT LIMITED TO, THE IMPLIED WARRANTIES OF MERCHANTABILITY AND FITNESS FOR A PARTICULAR PURPOSE ARE DISCLAIMED. IN NO EVENT SHALL THE COPYRIGHT OWNER OR CONTRIBUTORS BE LIABLE FOR ANY DIRECT, INDIRECT, INCIDENTAL, SPECIAL, EXEMPLARY, OR CONSEQUENTIAL DAMAGES (INCLUDING, BUT NOT LIMITED TO, PROCUREMENT OF SUBSTITUTE GOODS OR SERVICES; LOSS OF USE, DATA, OR PROFITS; OR BUSINESS INTERRUPTION) HOWEVER CAUSED AND ON ANY THEORY OF LIABILITY, WHETHER IN CONTRACT, STRICT LIABILITY, OR TORT (INCLUDING NEGLIGENCE OR OTHERWISE) ARISING IN ANY WAY OUT OF THE USE OF THIS SOFTWARE, EVEN IF ADVISED OF THE POSSIBILITY OF SUCH DAMAGE.

```

function [ f_rec , X ] = abel_inversion(h,R,upf,plot_results,lsq_solve)
% This function calculates a Fourier-based Abel inversion based on the
% method described in [1]. Assuming cylindrical symmetry, the distribution
% function f_rec can be reconstructed from the measured profile h .
%
% The main idea is a Fourier-series-like expansion of the unknown
% distribution function f(r) into
%  $f(r) = \sum_{n=lof}^{upf} (A_n * f_n(r))$ 
% (1)
% where the lower frequency is set to 1 and the upper frequency upf is
% important for noise-filtering.
%
%
% INPUT:  H - dataset to be analyzed (1xN - matrix).
%         For optimum results, H(1) should be the center and H(N) the
%         edge of the investigated object and H(N) should be approx
zero.
%         If no input H is given, a sampla dataset will be created.
%         R - radius of given system (i.e. distance between H(1) and H(N))
%         UPF - upper frequency limit. Defines the number of cosinus
%         expansions (and critically determines computation time).
%         Choosing a very low value (e.g. 4) results in a low-pass
%         filtering effect, reducing noise (but also potential features)
%         PLOT_RESULTS - set to 1 to plot the results
%         LSQ_SOLVE - set to 1 to use LSQCURVEFIT instead of algebraically
%         solving the least square problem - maybe useful if the
inversion
%         of a singular matrix occurs (I am not sure if this might
happen)
%
% OUTPUT: F_REC - reconstructed density profile
%         X - x-vector containing spatial coordinates for F_REC
%
%
% [1] G. Pretzler, Z. Naturforsch. 46a, 639 (1991)
%
% See also: COMPUTE_EXPANSION, GENERATE_TEST_DATA, SOLVE_LSQ
%
%
% written by C. Killer, Sept. 2013

%% format data / generate sample data

% create sample data based on a polynomial distribution function
% if no data input is given
if ~exist('h', 'var') || isempty(h)
    [X,h,R]=generate_test_data;
    plot_results=1;
else
    X=linspace(0,R,length(h));
end

% default value for number of expansion elements
if ~exist('upf', 'var'); upf=10; end;

% avoiding problems if flags are not given in input

```

```

if ~exist('plot_results', 'var'); plot_results=0; end;
if ~exist('lsq_solve', 'var'); lsq_solve=0; end;

%% calculate series expansions fn and corresponding integrals hn

[fn,hn] = compute_expansion( X,upf,R );

%% solve equation system A*L=B for the amplitudes A
if lsq_solve ~= 1

    B = zeros(1,upf+1); L = zeros(upf+1,upf+1); %create arrays

    for k=1:upf+1

        for l=1:upf+1
            L(l,k)=2.*sum(hn(:,k).*hn(:,l)); % January 2016: added factor
2
        end

        B(k)=sum(hn(:,k));
    end

    A=B/L;

else

    x0=1*ones(upf+1,1); % guess some initial values for optimisation
    A=solve_lsq(h,hn,x0); % solve for amplitudes A
end

%% final stage: calculate the resulting distribution profile

% create vector for resulting reconstructed distribution
f_rec=zeros(length(h),1);

% special case for n=0 (where f_0(r) = 1)
f_rec = f_rec + A(1)*1;

% iterate eq. (1) for n=1:upf
for c=2:upf+1
    f_rec = f_rec + A(c).*fn(:,c);
end

if plot_results==1
    figure; % normalized profiles for better comparison
    set(gca, 'linewidth',1.5, 'fontsize',16)
    hold on;
    plot(X,h./max(h), 'b', 'Linewidth',1.5);
    plot(X,f_rec./max(f_rec), 'k', 'Linewidth',1.5);
    grid on; box on;
    title(sprintf('number of cos-expansions: %i',upf))
    legend('measured profile','reconstructed
distribution','Location','SouthWest')
end

```

```

function [ fn,hn ] = compute_expansion( X,upf,R )
% COMPUTE_EXPANSION calculates the Fourier series expansion terms, on
which
% the Abel inversion algorithm [1] is based.
%
% Details: The unknown distribution f(r) is expanded as
%           f(r) = sum_{n=lof}^{upf} (A_n * f_n(r))           (1)
% where the lower frequency is set to 1 and the upper frequency upf is
% important for noise-filtering. f_n(r) is a set of cos-functions:
%           f_n(r) = 1 - (-1)^n*cos(n*pi*r/R) and f_0(r) = 1   (2)
% For the Abel inversion, the integrals h_n have to be calculated
%           h_n(x) = int_x^R f_n(r) * r / sqrt(r^2-x^2) dr     (3)
%
% [1] G. Pretzler, Z. Naturforsch. 46a, 639 (1991)
%
%                               written by C. Killer, Sept. 2013

% allocate matrices for f_n and h_n - rows are x-values,
% columns are the number of expansion elements (n+1 since we start with
n=0)
fn=zeros(length(X),upf+1);
hn=zeros(length(X),upf+1);

% special case: first column for n=0, where f_0(r)=1;
fn(:,1)=1;
for c=1:length(X);
    x=X(c);

    % evaluation of (3)
    fun = @(t) ones(size(t));
    hn(c,1) = integral(fun,0,sqrt(R^2-x^2));
end

% all the other columns
for n=1:upf
    for c=1:length(X)
        x=X(c);

        % evaluation of (2)
        fn(c,n+1) = (1 - (-1)^n*cos(n*pi*x/R));

        % evaluation of (3)
        fun=@(t) (1 - (-1)^n*cos(n*pi*sqrt(t.^2+x.^2)/R)).* ones(size(t));
        hn(c,n+1) = integral(fun,0,sqrt(R^2-x^2));
    end
end

% remove the next comment to plot the integrals
% figure; plot(hn); title('cos-expansion integrals h_n(x)')

```

```

function [ X,h,R ] = generate_test_data(~)
% GENERATE_TEST_DATA creates a sample data set for demonstration of the
% Abel inversion algorithm. Based on the density distribution f
% (polynomial function), the virtual measurement result h is calculated
% via Abel transform:
%
%           h(x) = 2* int_x^R f(r)*r/sqrt(r^2-x^2) dr           (1)
%
%
%
%
%                               written by C. Killer, Sept. 2013

R=3;                               % radius
X=(0:0.01:R-0.01)';                % spatial coordinates

%polynomial distribution function
f= (17.*(X./R).^4-32.*(X./R).^3+14.*(X./R).^2+1);

h=zeros(length(X),1);              % allocate result vector

for c=1:length(X)
    x=X(c);
    % evaluate Abel-transform equation (1)
    fun = @(r) (17.*(r./R).^4-32.*(r./R).^3+14.*(r./R).^2+1).*r./sqrt(r.^2
- x.^2);
    h(c,1)=2*integral(fun,x,R);
end

figure;
plot(X,f./max(f),'k','Linewidth',1.5);
hold on;
plot(X,h./max(h),'b','Linewidth',1.5);
grid on; box on;
legend('initial density distribution f(r)', 'measurement result h(r) (Abel-
Transform of f(r))', 'Location', 'SouthWest')
title('example with polynomial data sample (normalized for better
comparison)')

```

```

function [ A ] = solve_lsq( h,hn,x0 )
% The problem (sum_{k=1}^N (H(y_k) - h(y_k))^2 == min) has to be solved,
% where y_k are the N measured points, h is the measured data and
%  $H = 2 \cdot \sum_n (A_n \cdot hn(y))$  is the sum over the number of expansion elements
% of the expression  $A \cdot hn$  with the already computed integrals  $hn$  and the
% corresponding amplitudes  $A$ . [1]
%
% [1] G. Pretzler, Z. Naturforsch. 46a, 639 (1991)
%
% written by C. Killer, Sept. 2013

% function to be optimized
myfun=@(x,hn) 2*hn*x;

% let MATLAB do the least-square-calculation, resulting in the amplitudes
A
A=lsqcurvefit(myfun,x0,hn,h);

```